

RESEARCH ARTICLE

Energy-Efficient Cabin Climate Control of Electric Vehicles Using Linear Time-Varying Model Predictive Control[†]

Youyi Chen¹ | Kyoung Hyun Kwak¹ | Jaewoong Kim² | Youngki Kim*¹ | Dewey Jung¹¹Mechanical Engineering, University of Michigan-Dearborn, Michigan, USA²Hyundai-Kia Motor Company, Gyeonggi-do, South Korea**Correspondence**

*Youngki Kim, Mechanical Engineering, University of Michigan-Dearborn, Dearborn, MI 48128, USA Email: youngki@umich.edu

Abstract

A cabin climate control system, often referred to as a heating, ventilation, and air conditioning (HVAC) system, is one of the largest auxiliary loads of an electric vehicle, and the real-time optimal control of HVAC brings a significant energy-saving potential. In this paper, a linear-time-varying (LTV) model predictive control (MPC)-based approach is presented for energy-efficient cabin climate control of EVs. A modification is made to the cost function in the considered MPC problem to simplify the Hessian matrix in utilizing quadratic programming (QP) for real-time computation. A rigorous parametric study is conducted to determine optimal weighting factors that work robustly under various operating conditions. Then, the performance of the proposed LTV-MPC controller is compared against a rule-based (RB) controller and a nonlinear economic MPC (NEMPC) benchmark. Compared with the RB controller benchmark, the LTV-MPC reaches the target cabin temperature at least 69 s faster with 3.2 % to 15 % less HVAC system energy consumption, and the averaged cabin temperature difference is 0.7 °C at most. Compared with the NEMPC, the LTV-MPC controller can achieve comparable performance in temperature regulation and energy consumption with fast computation time, as compared to the NEMPC: the maximum differences in temperature and energy consumption are 0.4 °C and 2.6 %, respectively, and the computational time is reduced 72.4 % on average with the LTV-MPC.

KEYWORDS:

heating, ventilation, and air-conditioning (HVAC) control; vehicle thermal management; model predictive control; electric vehicles

1 | INTRODUCTION

The market share of electric vehicles (EVs) has increased noticeably during the past decades¹. Nonetheless, range anxiety, EV drivers' fear that battery state of charge (SOC) is too low to reach the desired destination, is still one of the concerns for the potential customers of EVs. They are more anxious about the SOC and the remaining range than current EV owners². Thus, improving the all-electric range (AER) of an EVs is essential for resolving lagging EV adoption. Among all the auxiliary components of the EVs, a vehicle cabin climate control system, which includes an air-conditioning (A/C) system and an electric heater, is accountable for the most significant energy consumption³. Due to the energy consumed by the cabin climate control, the average AER can be decreased by approximately 30 – 40 %, depending on vehicle types and driving scenarios^{4,5}. Therefore, optimizing the cabin climate control is essential for enhancing the AER performance of an EV.

[†]The authors from the University of Michigan-Dearborn would like to acknowledge the financial and technical support from Hyundai-Kia Motor Company.

This is the author manuscript accepted for publication and has undergone full peer review but has not been through the copyediting, typesetting, pagination and proofreading process, which may lead to differences between this version and the Version of Record. Please cite this article as doi:

This article is protected by copyright. All rights reserved.

In various practical scenarios, an A/C system and a heater may operate at the same time. For example, to avoid unpleasant odor from the evaporator outlet air, the temperature should be kept under a certain level⁶. In such a case, the A/C may over-cool, and the vent outlet air temperature will need to be heated to achieve a desired cabin air temperature. Moreover, in a dehumidification mode, the A/C is utilized to chill the airflow at the evaporator. In such cases, the outlet air from the evaporator may be too cold to be supplied directly to the cabin; therefore, a heating process, the so-called reheating operation, is required to warm up the chilled air^{7,8,9}. In an EV, an electric heater is typically utilized, and a more efficient heat pump option is also available¹⁰. However, these are far less efficient than a heater core using wasted heat from an internal combustion engine. Therefore, an optimal cabin climate control algorithm should consider cabin cooling and heating at the same time.

For vehicle cabin climate control, various control techniques have been introduced in the literature. A rule-based (RB) controller typically utilizes map-based control actions depending on given environmental conditions and various states as measured from the heating, ventilation, and air conditioning (HVAC) system of the vehicle cabin¹¹. The maps or rules for the control actions need to be pre-calibrated for given driving conditions and operating ranges. Therefore, this type of controller does not require any online optimization process, and hence the computational load is low. However, the RB controller does not ensure optimality in temperature regulation and energy minimization. Rostiti *et al.*¹² proposed an RB controller utilizing offline-solved dynamic programming in the process of rule calibration. This strategy offers control performance approaching the optimal temperature regulation and energy consumption of dynamic programming. However, the method still does not guarantee the optimal control trajectory in various driving scenarios. To pursue the robustness of the controller in various conditions, Zhang *et al.*¹³ applied an H_∞ control method to a vehicle A/C system. The H_∞ controller is constructed so that the H_∞ norm of the transfer function between the disturbance and the controlled output is as small as possible, which leads to better temperature trajectory tracking and disturbance rejection. However, energy consumption is not considered in the control design.

Recently, model predictive control (MPC) has become popular in addressing the vehicle climate control problem to achieve optimal temperature tracking and energy-saving performance. Optimal control is achieved by minimizing a cost function about the states and controls within a prediction horizon. For such an optimization process, the computational cost for the control-oriented model needs to be adequately reduced. The HVAC system is nonlinear and inherits the complexity of two-phase fluid dynamics, making MPC-based cabin climate control more challenging. Several studies have proposed approaches for reducing the order of the control-oriented model by utilizing the A/C system's setpoints as control inputs for the MPC problem; however, heating operation is typically ignored. Wang *et al.*^{14,15} developed a nonlinear MPC (NMPC), which is based on a phenomenological model of the evaporator, discharge temperature, and blower mass flow rate, to regulate cabin temperature with minimum energy consumption. This NMPC works as a high-level controller to determine the control settings of the climate control panel, such as blower level and temperature set point. However, the heating is not considered as well as the optimal control of the refrigerant cycle components. Glos *et al.*¹⁶ proposed an NMPC for an EV climate control system. In the considered system, the duct air for the cabin is cooled by a coolant circuit that is between the duct and refrigerant cycle. The heat transfer rate from the refrigerant cycle works as a control input, which reduces the computational burden greatly since the two-phase flow heat transfer is not calculated. The NMPC problem is solved to achieve optimal operation, including cabin temperature tracking, carbon dioxide, and energy saving. However, this NMPC also has similar drawbacks to the controllers in^{14,15}; the heating operation is not considered, and the A/C components such as the compressor and the fan are not optimally controlled.

The prediction model accuracy and control performance may be improved further by including a vapor compression cycle model in the MPC instead of estimating total energy consumption from cooling power demand. In our previous work¹⁷, a nonlinear economic MPC (NEMPC) is proposed for vehicle climate control with the cooperation of both air conditioner and heater. With the quasi-steady-state assumption, the vapor compression cycle and the cabin air dynamics are simplified to a three-state nonlinear model. The compressor and the fan mass flow rates and the heater power are included as control inputs for the optimal control of the HVAC system. The proposed controller shows outstanding performance in temperature tracking and energy saving under various driving scenarios.

However, the aforementioned NMPC controllers can still be computationally demanding; therefore, they are inadequate for real-time application with limited computational power. The computational load of the optimal cabin climate control problem can be dramatically reduced by using a linear MPC in the form of quadratic programming (QP), as many fast QP solvers have been developed for online implementation^{18,19}. In general, a highly nonlinear climate control model is converted into a linear model via linearization around a fixed point^{8,20,21,22}. Then, the original complex optimal control problems are transformed with the quadratic cost function into a QP problem. The linear MPC for the cabin climate control can demonstrate good temperature tracking and energy-saving performance comparable to NMPCs, and the computational time can be reduced by up to 10 to 15 times⁸. However, in the previous studies^{8,20,21,22}, the linearized model remains the same within the prediction horizon. In

transient cases where state and control trajectories could significantly vary, the performance of the LTI-MPC can be degraded due to the inaccurate prediction of the LTI model²³. Thus, a linear-time-varying (LTV)-MPC, which constructs the linearized prediction model multiple times within the prediction horizon, is utilized in this study to enhance the quality of the prediction and the performance of the QP-based optimal cabin climate control of EVs.

The LTV-MPC controller is designed to minimize the energy consumption of the HVAC system while regulating temperatures of the cabin air and evaporator outlet airflow. The main contribution of this paper is threefold:

- A QP-based LTV-MPC controller is proposed based on the nonlinear physics-based vehicle climate control problem proposed in our previous work¹⁷, and the detailed development process is presented. To simplify the Hessian matrix calculation by eliminating non-symmetric bi-linear terms, a modification to the compressor power consumption model is introduced and its effectiveness is evaluated.
- The impact of weighting factors on energy consumption and temperature regulation performance is thoroughly investigated and analyzed through extensive parametric studies in various driving scenarios including two ambient temperature conditions at 24 °C and 38 °C. Weighting factors for temperature tracking have different impacts on the control performance at different ambient temperatures. On the other hand, weighting factors for control rates work distinctively in different driving cycles.
- The performance of the LTV-MPC controller with optimal weighting factors is compared with the NEMPC in our previous work¹⁷. The proposed LTV-MPC has a temperature tracking and energy consumption difference of less than 0.3 °C and 2.6 %, respectively. Also, compared with an RB controller¹¹, the LTV-MPC shows a shorter time (more than 20 %) to reach the target temperature while using less energy (more than 5.1 %).

The rest of the paper is organized as follows: Section 2 presents the control-oriented model for cabin climate control. Section 3 presents the development of the proposed LTV-MPC, including model linearization, cost function, and constraints to the LTV-MPC. Section 4 discusses the results and analysis of the parametric study and the comparison against the NEMPC¹⁷ under three different driving cycles. The performance of the proposed LTV-MPC controller is evaluated under a validation driving cycle. The evaluation results are compared with the NEMPC and the RB controller¹¹. Finally, concluding remarks and discussion on future directions are given in Section 5.

2 | NONLINEAR CABIN CLIMATE CONTROL MODEL

In this section, the nonlinear control-oriented prediction model for the proposed LTV-MPC, which had been developed in our previous work¹⁷, is presented. A schematic diagram of the cabin climate control system considered in this study is illustrated in Fig. 1. As shown in the figure, the system consists of an A/C system and a vehicle cabin system. The cooled air from the evaporator of the A/C system is delivered to the cabin by a blower. Since the A/C system is kept running to regulate the evaporator at a low temperature for odor avoidance, an electric heater is utilized to warm up the cooled air to avoid cabin overcooling. The cabin air will be re-circulated to the evaporator, the amount of which is controlled by a re-circulation door. The modeling details of the two systems as well as their energy consumption are discussed in the following subsections 2.1, 2.2, and 2.3.

2.1 | Cabin modeling

The vehicle cabin is modeled using a lumped parameter method. Both the thermal dynamics of the cabin air and a pseudo vehicle component called the interior structure are calculated as lumped masses. The interior structure takes the heat transfer from the solar radiation (\dot{Q}_{solar}) and the ambient air (\dot{Q}_{amb}), and exchanges heat with the lumped cabin air (\dot{Q}_{int}). The lumped cabin air also has heat transfer with air cooled by the evaporator, which is heated before entering the cabin. The dynamics of the cabin

air temperature T_{cab} and the interior structure temperature T_{str} are described as follows:

$$\dot{T}_{cab} = \frac{1}{m_{cab}c_{p,a}} \left(\dot{m}_{blwr}c_{p,a}(T_{avo,k} - T_{cab}) + \dot{Q}_{int} \right), \quad (1)$$

$$\dot{T}_{str} = \frac{1}{C_{p,str}} \left(\dot{Q}_{solar} + \dot{Q}_{amb} - \dot{Q}_{int} \right), \quad (2)$$

$$T_{avo} = T_{aeo} + \frac{\dot{Q}_{htr}}{\dot{m}_{blwr}c_{p,a}} \quad (3)$$

$$\dot{Q}_{amb} = (a_1 V_{kph} + a_2)(T_{amb} - T_{str}), \quad (4)$$

$$\dot{Q}_{int} = (a_3 \dot{m}_{blwr} + a_4)(T_{str} - T_{cab}), \quad (5)$$

where T_{aeo} is the air temperature at the evaporator outlet, the dynamics of which are discussed in the following subsection 2.2; T_{avo} is the air temperature at the vent outlet; T_{amb} is the ambient temperature; \dot{Q}_{htr} is the heat transfer rate from the electric heater to the evaporator outlet airflow; \dot{m}_{blwr} is the air mass flow rate of the blower. The mass of the cabin air, the specific heat capacity for the air, and the heat capacity of the structure are denoted by m_{cab} , $c_{p,a}$, and $C_{p,str}$, respectively. \dot{Q}_{amb} and \dot{Q}_{int} are calculated with the overall thermal conductance, which are functions of the vehicle speed V_{kph} and the blower air mass flow rate \dot{m}_{blwr} respectively. \dot{Q}_{solar} is considered as a constant value in this study.

2.2 | A/C system modeling

The A/C system is modeled based on an ideal vapor-compression cycle assumption. Since the refrigerant flow transient response is much faster than the cabin thermal dynamics, the refrigerant flow is assumed to be quasi-steady and the evaporator heat transfer at the refrigerant side is calculated with a static energy balance equation. Meanwhile, at the air side, both the sensible heat transfer (temperature change) and latent heat transfer (humidity change) are considered. Therefore, the dynamics of the air temperature at the evaporator outlet T_{aeo} are described as follows:

$$\dot{T}_{aeo} = -\frac{1}{\tau_{aeo}}T_{aeo} + \frac{1}{\tau_{aeo}} \left(T_{abo} + \frac{\dot{m}_{comp}\Delta h}{\dot{m}_{blwr}c_{p,a}} + \frac{(\omega_i - \omega_e)h_{fg}}{c_{p,a}} \right), \quad (6)$$

$$\Delta h = f(\dot{m}_{comp}, \dot{m}_{fan}), \quad (7)$$

$$T_{abo} = r_{in}T_{cab} + (1 - r_{in})T_{amb}, \quad (8)$$

where \dot{m}_{comp} is the refrigerant mass flow rate of the compressor, \dot{m}_{fan} is the fan air mass flow rate, Δh is the refrigerant enthalpy difference between the evaporator inlet and outlet, T_{abo} is the blower outlet air temperature, r_{in} is the ratio of the return air mass flow to the ambient air mass flow. The absolute humidity of the evaporator inlet and outlet airflow is denoted by ω_i and ω_e , respectively, and h_{fg} is the latent heat of the water. Computing Δh in the thermodynamic cycle typically requires an iterative method due to its inherent recursive relationship with T_{aeo} . Therefore, Δh is calculated and its sensitivity to the refrigerant and air mass flow rates are investigated under a wide range of operating conditions including various ambient temperatures. Then Eq. (7) is developed as a regression model as a function of \dot{m}_{comp} and \dot{m}_{fan} to capture the response of the ideal vapor-compression

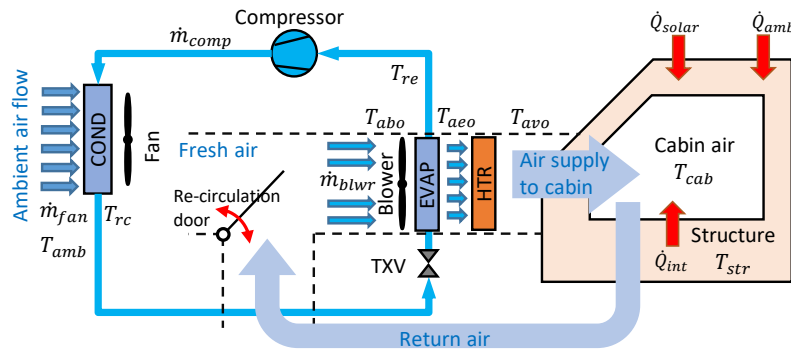


FIGURE 1 A schematic diagram of the considered cabin climate control system

cycle¹⁷. It is noted that for the T_{aeo} , a first-order filter with a time constant τ_{aeo} is used in Eq. (6) to capture any dynamics that are not modeled.

2.3 | Power consumption modeling

In this study, three components in the cabin climate control system are controlled, which are the compressor, the fan, and the electric heater. For energy consumption minimization, the power consumption of each component is modeled and used in the cost function in the MPC. The power consumption model is developed based on the performance test data of the components provided by the manufacturer. The compressor responses in a wide range of operating conditions are investigated, and the power consumption is expressed as a regression model. The fan power consumption model is regressed based on the numerical test data at different vehicle speeds to account for the ram-air effect by the vehicle frontal structure in a wide range of conditions. It is noted that the blower is controlled by an RB controller instead of the MPC because its settings are often manually adjusted by the driver or the passenger. Therefore, it is considered as a disturbance, and hence its power is not considered in the MPC formulation. The power consumption of the compressor, the fan, and the electric heater is expressed as follows:

$$P_{comp} = a_1 T_{re} \dot{m}_{comp} + a_2 \dot{m}_{comp}^2 + a_3 \dot{m}_{comp} + a_4 \dot{m}_{fan} \dot{m}_{comp}, \quad (9)$$

$$P_{fan} = a_5 \dot{m}_{fan}^2 + a_6 \dot{m}_{fan} + g(v), \quad (10)$$

$$P_{htr} = \dot{Q}_{htr} \quad (11)$$

$$T_{re} = T_{abo} - \epsilon_e^{-1} (T_{abo,k} - T_{aeo}), \quad (12)$$

where P_{comp} , P_{fan} , and P_{htr} are the power consumption of the compressor, the fan, and the heater, respectively; T_{re} is the refrigerant temperature at the evaporator; $g(v)$ is a function of the vehicle speed to account the ram-air effect; ϵ_e^{-1} is the inverse of the evaporator effectiveness, which is linearly regressed as a function of \dot{m}_{blwr} using the heat exchanger performance data.

3 | LTV-MPC CONTROLLER DEVELOPMENT

In this section, the development of the LTV-MPC for cabin climate control is discussed. The LTV-MPC is designed to regulate T_{cab} and T_{aeo} smoothly with minimum energy consumption. Because of the LTV prediction model and the quadratic cost function, the LTV-MPC can be converted into a QP problem and solved with relatively small computational burden. The following equations express the general form of the LTV-MPC problem, including a quadratic cost function, an LTV state evolution equation, and linear inequality constraints:

$$\begin{aligned} \min_{\Delta u_k} \quad & J = \sum_{k=0}^{N_h-1} (\xi_{k+1}^T Q \xi_{k+1} + \Delta u_k^T R \Delta u_k + q_\xi \xi_{k+1}), \\ \text{s.t.} \quad & \xi_{k+1} = A_{aug,k} \xi_k + B_{aug,k} \Delta u_k + D_k, \\ & E_\xi \xi_k \leq F_{\xi,k}, \\ & E_{\Delta u} \Delta u_k \leq F_{\Delta u}, \end{aligned} \quad (13)$$

where J is the cost function, k is the discrete-time index, N_h is the number of prediction steps, ξ is the augmented system state vector, and Δu is the augmented system control input vector. The system states are evolved in an LTV prediction model while the state and control input vectors follow linear constraints in the prediction horizon. The system is expressed in an augmented form, with the increment of the control variables (\dot{m}_{comp} , \dot{m}_{fan} , and \dot{Q}_{htr}) as the control inputs, so that constraints and cost function terms for the rate of control inputs can be applied.

In the following subsections, the details of the augmented LTV model, the cost function, and the constraints are discussed. Then, the optimization problem is expressed in a QP form.

3.1 | The Augmented LTV Model

The nonlinear model discussed in Section 2 is linearized for the LTV-MPC. For simplicity, the nonlinear equations (1), (2), and (6) are expressed as follows:

$$\begin{aligned}
\dot{x}_k &= f(x_k, u_k, d_k), \\
x_k &= [T_{cab,k}, T_{aao,k}, T_{str,k}]^T, \\
u_k &= [\dot{m}_{comp,k}, \dot{m}_{fan,k}, \dot{Q}_{htr,k}, \epsilon_{aao,k}, \epsilon_{fan,k}]^T, \\
d_k &= [V_{kph,k}, \dot{m}_{blwr}, T_{amb}, \dot{Q}_{solar}, r_{in}, \omega_i, \omega_e]^T,
\end{aligned} \tag{14}$$

where x and u are state vector and control input vector; d is the disturbance vector; ϵ_{aao} and ϵ_{fan} are the slack variables for the T_{aao} regulation and the fan-related soft constraints, which will be discussed in subsection 3.3. It is noted that accurate information about vehicle speed V_{kph} is assumed to be available and kept updated in the prediction horizon, similar to the approaches used by Wang *et al.*¹⁴ and Amini *et al.*²⁴.

The other disturbances are kept constant in the prediction horizon. At an operating point, in the prediction horizon, (x_l, u_l, d_l) , the nonlinear model is linearized and discretized as follows:

$$x_{k+1} = x_k + \Delta t \left. \frac{\partial f}{\partial x_k} \right|_{(x_l, u_l, d_l)} (x_k - x_l) + \Delta t \left. \frac{\partial f}{\partial u_k} \right|_{(x_l, u_l, d_l)} (u_k - u_l) + \Delta t \cdot f(x_l, u_l, d_l), \tag{15}$$

where Δt is the sampling time of the discretization.

When the nonlinear model is linearized in the LTV-MPC formulation using Eq. (15), a sequence of multiple linearization points, $\{(x_{0,k}, u_{0,k}, d_{0,k}), \dots, (x_{N_h-1,k}, u_{N_h-1,k}, d_{N_h-1,k})\}$, is needed. This sequence of linearization points is obtained as follows: (i) the estimated control trajectory for the k -th step is obtained by shifting the optimal control trajectory at the $(k-1)$ -th step, $\{u_{0,k-1}, u_{1,k-1}, \dots, u_{N_h-1,k-1}\}$, one step forward to $\{u_{1,k-1}, u_{2,k-1}, \dots, u_{N_h-1,k-1}, u_{N_h-1,k-1}\}$; (ii) the estimated states sequence, $\{x_{1,k}, x_{2,k}, \dots, x_{N_h,k}\}$, is obtained by applying the estimated control trajectory at the k -th step to the k -th states, $x_{0,k}$, using the nonlinear model (with disturbances updated); (iii) finally, the estimated state sequence and the estimated control trajectory at the k -th step are combined to form the sequence of linearization points.

For smooth operation, constraints on the rate of control input are considered in the LTV-MPC formulation. For convenience, the system is augmented to a velocity form by substituting $u_k = v_{k-1} + \Delta u_k$ for u_k as follows:

$$\begin{aligned}
v_{k-1} &= [\dot{m}_{comp,k-1}, \dot{m}_{fan,k-1}, \dot{Q}_{htr,k-1}, 0, 0]^T, \\
\Delta u_k &= [\Delta \dot{m}_{comp,k}, \Delta \dot{m}_{fan,k}, \Delta \dot{Q}_{htr,k}, \epsilon_{aao,k}, \epsilon_{fan,k}]^T.
\end{aligned} \tag{16}$$

Since the last two elements in v_{k-1} are 0, we can replace v_{k-1} by a three-element vector, v_{k-1} .

$$v_{k-1} = [\dot{m}_{comp,k-1}, \dot{m}_{fan,k-1}, \dot{Q}_{htr,k-1}]^T. \tag{17}$$

Then linearization point (x_l, u_l, d_l) becomes $(x_l, v_{l-1} + \Delta u_l, d_l)$, and the linearized system is expressed as follows:

$$x_{k+1} = A_k x_k + \bar{B}_k v_{k-1} + B_k \Delta u_k + \delta_k, \tag{18}$$

with

$$\begin{aligned}
A_k &= \Delta t \left. \frac{\partial f}{\partial x_k} \right|_{(x_l, u_l, d_l)} + I_{3 \times 3}, \\
B_k &= \Delta t \left. \frac{\partial f}{\partial u_k} \right|_{(x_l, u_l, d_l)}, \\
\bar{B}_k &= \Delta t \left. \frac{\partial f}{\partial v_k} \right|_{(x_l, v_l, d_l)}, \\
\delta_k &= -\Delta t \left(\left. \frac{\partial f}{\partial u_k} \right|_{(x_l, u_l, d_l)} u_l + \left. \frac{\partial f}{\partial x_k} \right|_{(x_l, u_l, d_l)} x_l \right) + \Delta t \cdot f(x_l, u_l, d_l).
\end{aligned}$$

Equation (18) is further expressed with an augmented state vector $\xi_k = [x_k, v_{k-1}]^T$, and the augmented system expressed in Eq. (19) is used in the LTV-MPC controller as follows:

$$\xi_{k+1} = A_{aug,k} \xi_k + B_{aug,k} \Delta u_k + D_k, \tag{19}$$

with

$$\begin{aligned} A_{aug,k} &= \begin{bmatrix} A_k & \bar{B}_k \\ 0_{3 \times 3} & I_{3 \times 3} \end{bmatrix}, \\ B_{aug,k} &= \begin{bmatrix} B_k \\ I_{3 \times 3} & 0_{3 \times 2} \end{bmatrix}, \\ D_k &= \begin{bmatrix} \delta_k \\ 0_{3 \times 1} \end{bmatrix}. \end{aligned}$$

3.2 | Cost Function

In this study, the objective of cabin climate control is to minimize the energy consumption and to regulate the temperatures. The cost function is expressed as follows:

$$\begin{aligned} J = \sum_{k=0}^{N_h-1} & \left(\frac{1}{2} \alpha_{T_{cab}} (T_{cab,k+1} - T_{cab,target})^2 + \frac{1}{2} \alpha_{T_{aero}} \epsilon_{T_{aero,k}}^2 + \frac{1}{2} \alpha_{fan} \epsilon_{fan,k}^2 \right. \\ & \left. + \tilde{P}_{comp,k} + P_{fan,k} + P_{htr,k} + \frac{1}{2} \alpha_{\Delta comp} \Delta \dot{m}_{comp,k}^2 + \frac{1}{2} \alpha_{\Delta fan} \Delta \dot{m}_{fan,k}^2 + \frac{1}{2} \alpha_{\Delta htr} \Delta \dot{Q}_{htr,k}^2 \right), \end{aligned} \quad (20)$$

where α s indicate weighting factors used for the different cost terms and Δ indicates the increment of the control inputs (the rate of the control inputs). The first term handles the T_{cab} regulation. The second and third terms are used for penalizing slack variables of the T_{aero} and \dot{m}_{fan} constraints. The fourth, fifth, and sixth terms represent the power consumption of the controlled components. The rest are for penalizing the rate of the control inputs. It is noted that a small weighting factor for \dot{Q}_{htr} is introduced just to ensure that the Hessian matrix is positive definite.

To obtain a symmetric cost function and further reduce the matrix complexity, a modification is made to the compressor power consumption. In Eq. (9), $P_{comp,k}$ is not a symmetric quadratic function because $T_{re,k}$ at the k -th step is multiplied by the state, $\dot{m}_{comp,k}$ at the $(k+1)$ -th step, which belongs to ξ_{k+1} in Eq. (19). Therefore, the first term in Eq. (9) is calculated by $T_{re,k}(\dot{m}_{comp,k-1} + \Delta \dot{m}_{comp})$. Although $T_{re,k} \dot{m}_{comp,k-1}$ can be expressed as a quadratic term of ξ_k , additional matrix calculation is necessary for the non-symmetric bi-linear term $T_{re,k} \Delta \dot{m}_{comp}$, which increases the computational burden. This issue can be resolved if the intermediate variable $T_{re,k}$ is shifted one step forward to $T_{re,k+1}$, with the result that the term $T_{re,k+1} \dot{m}_{comp,k}$ is expressed as a quadratic term of ξ_{k+1} . The modified compressor power $\tilde{P}_{comp,k}$ is expressed as follows:

$$\tilde{P}_{comp,k} = a_1 T_{re,k+1} \dot{m}_{comp,k} + a_2 \dot{m}_{comp,k}^2 + a_3 \dot{m}_{comp,k} + a_4 \dot{m}_{fan,k} \dot{m}_{comp,k} \quad (21)$$

Since the compressor power consumption is used as one of the cost terms, with properly tuned weighting factors the overall cost function shape will not be significantly affected as long as the compressor power trend is captured. To examine the impact of the shifting strategy on the power consumption accuracy, P_{comp} from the two methods are compared in an open-loop simulation with given control trajectories in various driving conditions. The temporal trends of P_{comp} , T_{re} difference ($= T_{re,k+1} - T_{re,k}$) and the P_{comp} error ($= (\tilde{P}_{comp} - P_{comp})/P_{comp}$) are evaluated as shown in Fig. 2(a)–(d). The simulations are based on three driving cycles, the urban dynamometer driving schedule cycle (UDDS), the highway fuel economy test cycle (HWFET), and the US06 driving cycle, and two ambient temperatures, 24 °C and 38 °C. As can be seen from Fig. 2(a) and (b), the trend of P_{comp} by the shifted method follows that of the original compressor power. The largest error is observed only during the initial period for about 30 s because of the T_{re} error swing shown in Fig. 2(c) in that period. Then, the T_{re} difference in Fig. 2(c) is kept within ± 2 °C after 30 s. The corresponding P_{comp} error in Fig. 2(d) is less than ± 10 % overall, but the error reduces to ± 5 % after the initial period. The T_{re} difference is kept within ± 2 °C after 30 s. The corresponding P_{comp} error is less than ± 10 %. The T_{re} difference becomes almost zero after 100 s, as does the P_{comp} error. Therefore, this strategy allows for exploiting a QP formulation without significant sacrifice in prediction accuracy.

3.3 | Constraints

The inequality constraints considered in the control problem are (i) the upper and lower bounds of the evaporator air temperature, (ii) the feasible zones of the compressor and fan operation, (iii) the upper and lower bounds of the compressor mass flow rate at different refrigerant temperatures, and (iv) the range of control input u_k , including their rate Δu_k .

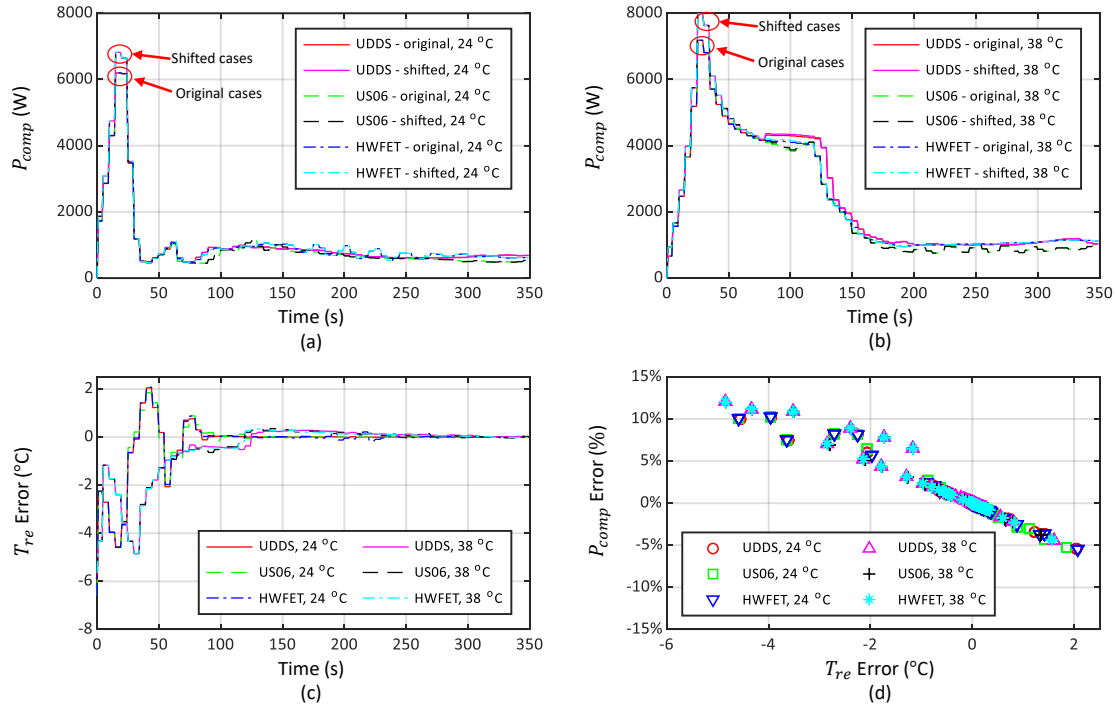


FIGURE 2 Temporal trends of original P_{comp} and shifted P_{comp} at T_{amb} of (a) 24 °C and (b) 38 °C, (c) temporal trends of T_{re} difference and (d) corresponding P_{comp} error.

By applying identical upper and lower bounds, T_{aeo} is regulated using a slack variable to a reference range, which is between T_{aeo}^{min} and T_{aeo}^{max} , to prevent unpleasant odor. In addition, to prevent ice accretion on the evaporator, T_{aeo} is maintained above 0 °C.

$$\begin{aligned} T_{aeo}^{min} - \epsilon_{T_{aeo}} &\leq T_{aeo,k+1} \leq T_{aeo}^{max} + \epsilon_{T_{aeo}}, \\ 0 &\leq T_{aeo,k+1}, \end{aligned} \quad (22)$$

The feasible zone of the compressor and the fan operations is constrained by six linear inequality equations to maintain the ideal vapor-compression cycle assumption. A high-fidelity MATLAB/Simulink component model based on the performance test data of the compressor is used to generate raw data in wide operating ranges at different ambient temperatures. Then, the feasible zone under the ideal cycle assumption is determined, as illustrated in Fig. 3. The boundaries of the zone are expressed as follows:

$$b_{1,j} \dot{m}_{fan,k} + b_{2,j} \dot{m}_{comp,k} + b_{3,j} \leq 0, \quad j = 1, \dots, 6, \quad (23)$$

where the coefficients $b_{1,j}$, $b_{2,j}$, and $b_{3,j}$ are determined based on the ambient temperature.

The compressor mass flow rate varies depending on the inlet refrigerant temperature of the compressor, $T_{re,k}$. Therefore, two additional constraints are used:

$$b_4 T_{re,k} - \dot{m}_{comp,k} \leq b_5, \quad (24a)$$

$$b_6 T_{re,k} + \dot{m}_{comp,k} \geq b_7. \quad (24b)$$

Considering physical limitations for the HVAC system components, box constraints are applied to the control inputs as shown in Eq. (25).

$$\dot{m}_{comp,k}^{min} \leq \dot{m}_{comp,k} \leq \dot{m}_{comp,k}^{max} \quad (25a)$$

$$\dot{m}_{fan,k}^{min} - \epsilon_{fan,k} \leq \dot{m}_{fan,k} \leq \dot{m}_{fan,k}^{max} + \epsilon_{fan,k} \quad (25b)$$

$$0 \leq \dot{Q}_{htr,k} \leq \dot{Q}_{htr,k}^{max}, \quad (25c)$$

To account for the ram-air effect from the vehicle frontal structure, $\dot{m}_{fan,k}^{min}$ and $\dot{m}_{fan,k}^{max}$ are calculated based on the vehicle speed. It is noted that the fan mass flow rate is limited by a soft constraint with a slack variable, which avoids numerical feasibility issues raised by dramatic vehicle velocity changes.

The rate of the control inputs and the slack variables are also constrained as follows:

$$\Delta \dot{m}_{comp,k}^{min} \leq \Delta \dot{m}_{comp,k} \leq \Delta \dot{m}_{comp,k}^{max}, \quad (26a)$$

$$\Delta \dot{m}_{fan,k}^{min} \leq \Delta \dot{m}_{fan,k} \leq \Delta \dot{m}_{fan,k}^{max}, \quad (26b)$$

$$\Delta \dot{Q}_{htr,k}^{min} \leq \Delta \dot{Q}_{htr,k} \leq \Delta \dot{Q}_{htr,k}^{max}, \quad (26c)$$

$$0 \leq \epsilon_{T_{aco},k}, \quad (26d)$$

$$0 \leq \epsilon_{fan,k}. \quad (26e)$$

3.4 | LTV-MPC formulated in the QP form

With the linearized system, quadratic cost function, and linear inequality constraints, the LTV-MPC problem formulated in Eq. (13) can be converted into a QP form as follows:

$$\begin{aligned} \min_U J &= \theta^T \tilde{Q} \theta + U^T \tilde{R} U + \tilde{q}_\xi \theta \\ &= \frac{1}{2} (U^T H U + 2q^T U + c), \\ \text{s.t. } GU &\leq W + T \xi_0, \end{aligned} \quad (27)$$

where the stacked state vector is expressed with the stacked control and residual constant vectors given by:

$$\theta = S U + M \xi_0 + C \Phi, \quad (28)$$

with

$$\begin{aligned} \theta &= [\xi_1 \ \xi_2 \ \dots \ \xi_{N_h}]^T, \\ U &= [\Delta u_0 \ \Delta u_1 \ \dots \ \Delta u_{N_h-1}]^T, \\ \Phi &= [D_0 \ D_1 \ \dots \ D_{N_h-1}]^T. \end{aligned} \quad (29)$$

It is noted that the Hessian matrix is checked to be positive definite for all the cases with simulations, which ensure the cost function is convex. The details of derivation can be found in the Appendices.

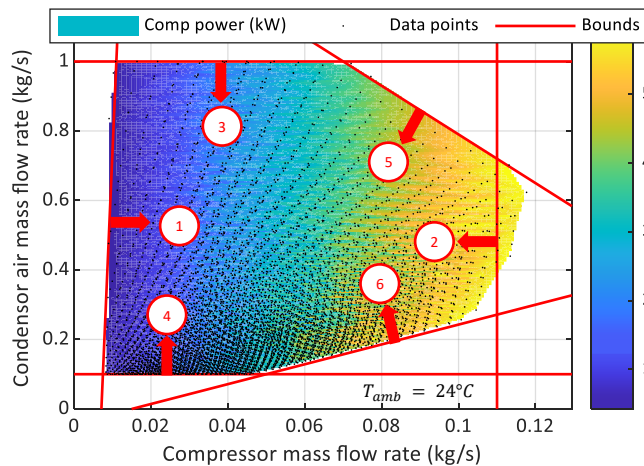


FIGURE 3 The feasible zone for \dot{m}_{comp} and \dot{m}_{fan} and approximated linear inequality constraints illustrated on the compressor power consumption under the ideal vapor-compression cycle operation at T_{amb} of 24 °C

4 | SIMULATION RESULTS AND DISCUSSION

This section presents the results of a parametric study of weighting factors and a performance evaluation of the proposed LTV-MPC control strategy. Since the performance of the MPC-based control strategy depends on the weighting factors in Eq. (20), it is important to determine their optimal values that work for various operating conditions. To this end, a parametric study is conducted with consideration of different driving cycles and ambient temperatures. More specifically, this study considers three driving cycles, the UDDS, the HWFET, and the US06 driving cycles shown in Figs. 4 (a), (b), and (c), and two ambient temperatures, 24 °C and 38 °C. In the parametric study, full factorial combinations of the weighting factors create different cost function shapes, influencing the preference and performance of the LTV-MPC controller. These full factorial combinations are tested in simulations, and the results are analysed and compared with each other. Based on the result of the parametric study, an optimal set of the weighting factors is chosen for the performance evaluation under various driving cycles, including the worldwide harmonized light vehicles test cycle (WLTC) shown in Fig. 4 (d) as a validation cycle.

The proposed LTV-MPC controller is implemented in a high-fidelity MATLAB/Simulink[®] plant model^{11,25} for vehicle simulations. The LTV-MPC problem is solved by using qpOASES²⁶ in the form of QP shown in Eq. (27). All the simulations are executed on a laptop with a 2.8 GHz processor. In this study, some parameters of the LTV-MPC are set as constants for all simulations: (1) the prediction horizon is 100 s; (2) the LTV-MPC sampling time is 5 s; (3) the LTV-MPC update time is 5 s; (4) the weighting factor for the slack variable on the fan bounds, α_{fan} , is 1×10^9 ; (5) the weighting factor, $\alpha_{\Delta hr}$, is set as a small value 1×10^{-4} for a positive-definite Hessian matrix, as is discussed in Section 3.2; (6) both T_{aero}^{min} and T_{aero}^{max} are set as 6 °C for simplicity. The prediction horizon is also tested over 200 s and 300 s with simulations, and the performance is not improved noticeably. Considering the much smaller computational burden, 100 s is selected as the horizon length. Similarly, the sampling time and update time are also tested with 1 s and 3 s and chosen as 5 s because of computational burden. The weighting factor of the fan soft constraint, α_{fan} , is determined as a large value by multiple tests so that the fan operation is properly constrained. It is also noted that the vehicle is assumed to be soaked in the ambient temperature at the initial point of the simulations. Therefore, the initial cabin temperature is set as $T_{amb} + 5$ °C due to the solar load.

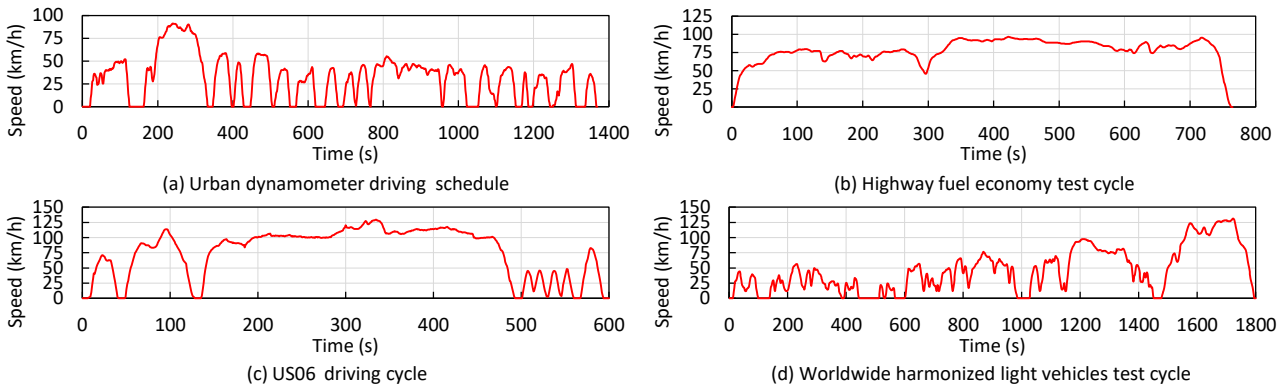


FIGURE 4 Driving cycles used in the simulation

4.1 | A Parametric Study: Weighting Factors for Reference Tracking

This subsection reports the results of the parametric study, which investigates the impact of two weighting factors on reference tracking. The simulation cases are generated by a full factorial combination of $\alpha_{T_{cab}}$ and $\alpha_{T_{aero}}$:

$$\alpha_{T_{cab}} \in \{1 \times 10^2, 2.5 \times 10^2, 5 \times 10^2, 7.5 \times 10^2, 1 \times 10^3, 2.5 \times 10^3, 5 \times 10^3\},$$

$$\alpha_{T_{aero}} \in \{1 \times 10^3, 2.5 \times 10^3, 5 \times 10^3, 7.5 \times 10^3, 1 \times 10^4, 2.5 \times 10^4, 5 \times 10^4\}.$$

The two other weighting factors in Eq. (20), such as $\alpha_{\Delta comp}$ and $\alpha_{\Delta fan}$, are set and kept constant to 1×10^2 and 1×10^3 , respectively. These weighting factors are set to mimic control trajectories of NEMPC¹⁷.

Figure 5(a) shows the average T_{cab} evaluated from the time when T_{cab} cools down to $T_{cab,target}$ for the first time at t_c to the end of each simulation. As expected, by increasing $\alpha_{T_{cab}}$, the average T_{cab} approaches the target; however, it is not sensitive to the $\alpha_{T_{aeo}}$. Figure 5(b) shows the average T_{aeo} , which is also evaluated from t_c to the end of each simulation. Although the overall variation of the average T_{aeo} is small, it becomes close to the target of 6 °C, predominantly by a larger $\alpha_{T_{aeo}}$. In general, the average values of T_{cab} and T_{aeo} in the 38 °C cases are not as close to the target temperature as in the 24 °C cases. This trend is due to the fact that the energy consumption is much larger in the 38 °C cases, which overweights temperature regulation terms in the cost function. Figures 5(c) and (d) show the cool-down time t_c and total energy consumption results. In the cases of T_{amb} at 24 °C, t_c and the overall energy consumption increase as $\alpha_{T_{cab}}$ increases; however, they are not very sensitive to $\alpha_{T_{aeo}}$. On the other hand, in the cases of higher T_{amb} at 38 °C, t_c is shorter with larger $\alpha_{T_{cab}}$ paired with smaller $\alpha_{T_{aeo}}$ and vice versa. Unlike T_{amb}

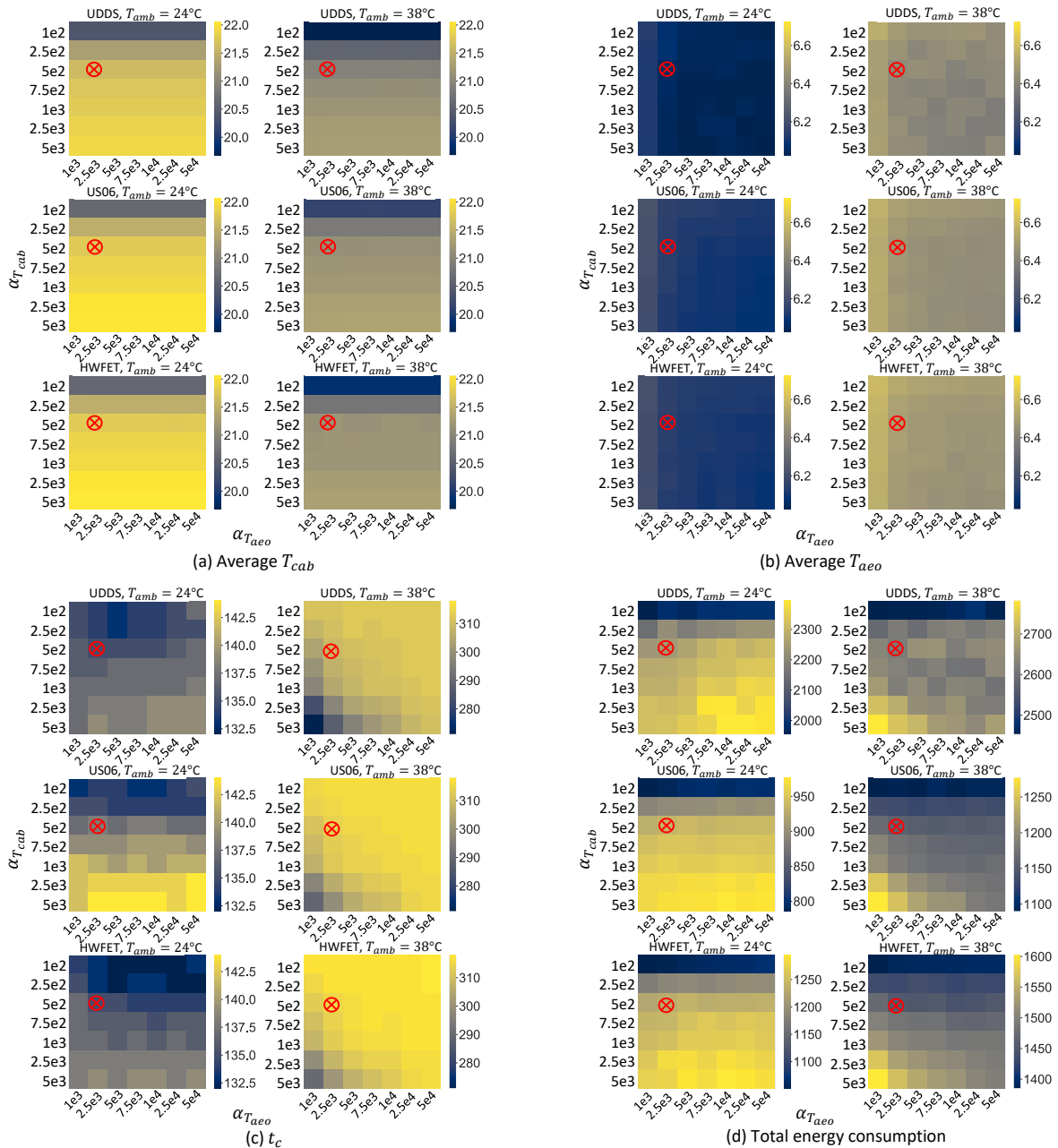


FIGURE 5 Parametric study results of $\alpha_{T_{cab}}$ and $\alpha_{T_{aeo}}$: (a) average T_{cab} , (b) average T_{aeo} , (c) t_c , and (d) total energy consumption. The red marks represent the selected parameter combination.

at 24 °C case, higher overall energy consumption is clearly observed with shorter t_c . To illustrate the influence of the weighting factors in detail, the temperature and control trajectories of four corner cases are shown and discussed. These four cases are selected because the combination of the boundary values of the weighting factors gives the most notable differences.

To analyze the observed average temperature trends in details, temperature and control trajectories are investigated for the four selected sets of weighting factors:

- Case (1): $\alpha_{T_{cab}} = 1 \times 10^2 / \alpha_{T_{aeo}} = 1 \times 10^3$,
- Case (2): $\alpha_{T_{cab}} = 1 \times 10^2 / \alpha_{T_{aeo}} = 5 \times 10^4$,
- Case (3): $\alpha_{T_{cab}} = 5 \times 10^3 / \alpha_{T_{aeo}} = 1 \times 10^3$,
- Case (4): $\alpha_{T_{cab}} = 5 \times 10^3 / \alpha_{T_{aeo}} = 5 \times 10^4$.

Figures 6(a)–(e) show the comparison of the four cases at T_{amb} of 24 °C until 400 s under the UDDS. In Fig. 6(a), T_{cab} trajectories are also predominantly influenced by $\alpha_{T_{cab}}$ but not by $\alpha_{T_{aeo}}$. The trajectories of the cases (1) and (2) are almost indistinguishable from each other, as are cases (3) and (4). On the other hand, all of the trajectories of T_{aeo} shown in Fig. 6(b) are very close to each other. These observations in the temperature trajectories can be explained by control actions shown in Figs. 6(c)–(d). When $\alpha_{T_{cab}}$ is small (case (1) and case (2)), the heater is actively used 50 s later, and the power trajectories are also lower than the other two cases. In comparison, the compressor and fan operations from all four cases are similar to each other. Specifically, once T_{aeo} is saturated to the target temperature, the compressor and fan operations are almost identical for all cases and approaches the lower bounds, especially for the compressor. The fan operation stays around 0.25 to 0.3 kg/s until the lower bound increases due to the ram-air effect at high vehicle speed. The compressor and fan operations of the four cases show that the target T_{aeo} can be achieved with the compressor operation near the low bounds. Maintaining the target T_{aeo} with the RB controlled blower operation in this intermediate ambient temperature condition overcools the cabin. Therefore, the heater is the main control action for the T_{cab} regulation. As $\alpha_{T_{cab}}$ decreases, the relative cost of the HVAC power consumption increases;

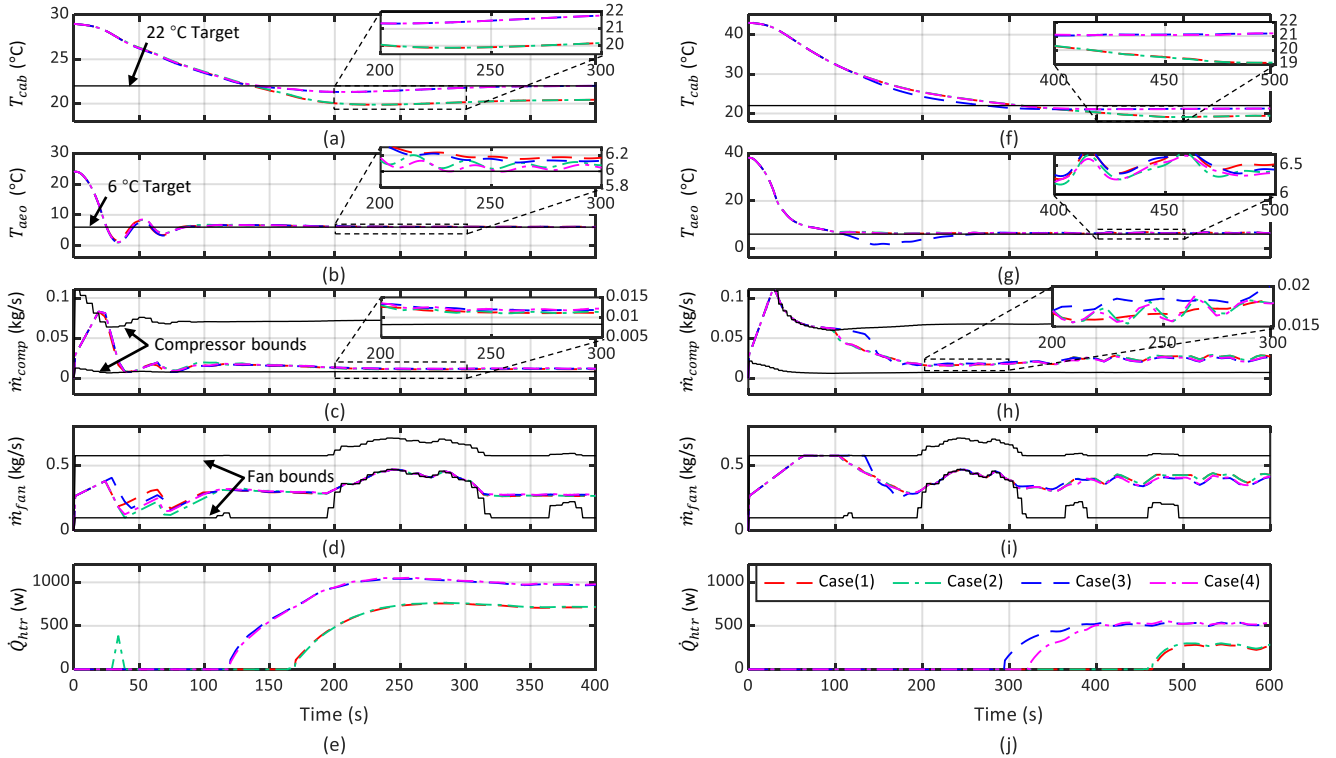


FIGURE 6 Temperature and Control Trajectories under the UDDS cycle for the four cases: (a)–(e) at T_{amb} of 24 °C and (f)–(j) at T_{amb} of 38 °C

thus, lowering the heater usage is the resulting optimal solution from the LTV-MPC. As a result, T_{cab} and the cool-down time become lower by approximately 2 °C and longer by 5 s, respectively.

Figures 6 (f)–(j) show the comparison of the four cases at T_{amb} of 38 °C until 600 s under the UDDS. In cases (1), (2), and (4), the temperatures, compressor, and fan trajectories are very similar to each other. In case (3), when $\alpha_{T_{cab}}$ is larger than $\alpha_{T_{aeo}}$, the compressor and the fan are used at their maximum limits until about 130 s, longer than the other cases. This operation causes undershooting of T_{aeo} as shown in Fig. 6(g), which leads to the slightly faster T_{cab} cool-down. Therefore, the heater is used early in case (3) to compensate the T_{aeo} undershooting; then, T_{aeo} is stabilized to the same level as observed in case (4). It should be noted that the blower setting by the RB controller is higher than the optimal setting. As a result, the A/C system still overcools the cabin slightly, and the heater is utilized, which is used more with larger $\alpha_{T_{cab}}$, although the heater power is about half compared to T_{amb} of 24 °C.

The parametric study in this subsection can be summarized as follows:

- In general, larger $\alpha_{T_{cab}}$ leads to better T_{cab} regulation and higher heater utilization, while larger $\alpha_{T_{aeo}}$ leads to better T_{aeo} regulation.
- The temperature regulation in the 38 °C cases is not as good as in the 24 °C cases because much higher energy consumption compromises temperature regulation in the 38 °C cases.
- In the 24 °C cases, the A/C system overcools the cabin even with the minimum operation of the compressor and fan. Only the heater is affected by $\alpha_{T_{cab}}$, which further influences T_{cab} regulation.
- In the 38 °C cases, the compressor, the fan, and the heater will be utilized more for T_{cab} regulation, if $\alpha_{T_{cab}}$ is larger than $\alpha_{T_{aeo}}$. Even in 38 °C cases, the heater is used because the A/C system overcools the cabin with the blower setting.

Considering the reference temperature tracking performance, $\alpha_{T_{cab}}$ can be as small as 5×10^2 for both temperatures to keep the average T_{cab} above 21 °C, but $\alpha_{T_{aeo}}$ can be any value to keep T_{aeo} within ± 1 °C from the target, although at 1×10^3 , the temperature increase is noticeable. Although optimal $\alpha_{T_{cab}}$ depends on the ambient temperature, lower $\alpha_{T_{aeo}}$ is preferred for faster cool-down, especially at T_{amb} of 38 °C. When $\alpha_{T_{cab}}$ is 5×10^2 , the total energy consumption is not very sensitive to $\alpha_{T_{aeo}}$ even at T_{amb} of 38 °C. Based on this result, $\alpha_{T_{cab}} = 5 \times 10^2$ and $\alpha_{T_{aeo}} = 2.5 \times 10^3$ are selected for the following parametric study and performance evaluation. The selected combination is highlighted with a red mark in Fig. 5.

4.2 | Parametric Study: Weighting Factors for Control Rate

This subsection reports the results of the parametric study, which investigates the impact of weighting factors on the control rate for smooth control actions. These weighing factors could affect the control performance, such as reference tracking and minimizing the total energy consumption. Among the three weighing factors, $\alpha_{\Delta_{comp}}$ and $\alpha_{\Delta_{fan}}$ are varied but $\alpha_{\Delta_{htr}}$ is still kept constant at 10^{-4} . For this parametric study, simulation cases are generated by a full factorial combination:

$$\begin{aligned}\alpha_{\Delta_{comp}} &= \{0.1, 1, 10, 1 \times 10^2, 1 \times 10^3, 1 \times 10^4, 1 \times 10^5, 1 \times 10^6, 1 \times 10^7, 1 \times 10^8\}, \\ \alpha_{\Delta_{fan}} &= \{1, 10, 1 \times 10^2, 1 \times 10^3, 1 \times 10^4, 1 \times 10^5, 1 \times 10^6\}.\end{aligned}$$

Figure 7(a) shows the average T_{cab} evaluated from t_c to the end of the simulation. For T_{amb} at both 24 °C and 38 °C, the two weighting factors do not affect the average T_{cab} , although there exists a variation of the average temperature depending on different driving cycles and T_{amb} . Figure 7(b) shows that the average T_{aeo} is essentially insensitive to $\alpha_{\Delta_{comp}}$ and $\alpha_{\Delta_{fan}}$ except for the largest end of $\alpha_{\Delta_{comp}}$. Figures 7(c) and (d) show the cool-down time t_c and total energy consumption results. The cool-down time t_c tends to be insensitive to the weighting factors; however, t_c becomes slightly shorter with the higher weighting factors at T_{amb} of 24 °C. On the other hand, at T_{amb} of 38 °C, t_c become slightly longer at the higher $\alpha_{\Delta_{comp}}$. The total energy consumption does not exhibit any specific trends in T_{amb} of either 24 °C or 38 °C. However, at the highest $\alpha_{\Delta_{comp}}$, the total energy consumption decreases slightly under the US06 and the HWFET. Under the UDDS, lower energy consumption is pronounced when both $\alpha_{\Delta_{comp}}$ and $\alpha_{\Delta_{fan}}$ are extremely high. Similar to the parametric study in the previous section, four sets of weighting factors in the corner cases are used to analyze the observed average temperature trends in detail:

- Case (1) $\alpha_{\Delta_{fan}} = 1/\alpha_{\Delta_{comp}} = 0.1$,
- Case (2) $\alpha_{\Delta_{fan}} = 1/\alpha_{\Delta_{comp}} = 1 \times 10^8$,

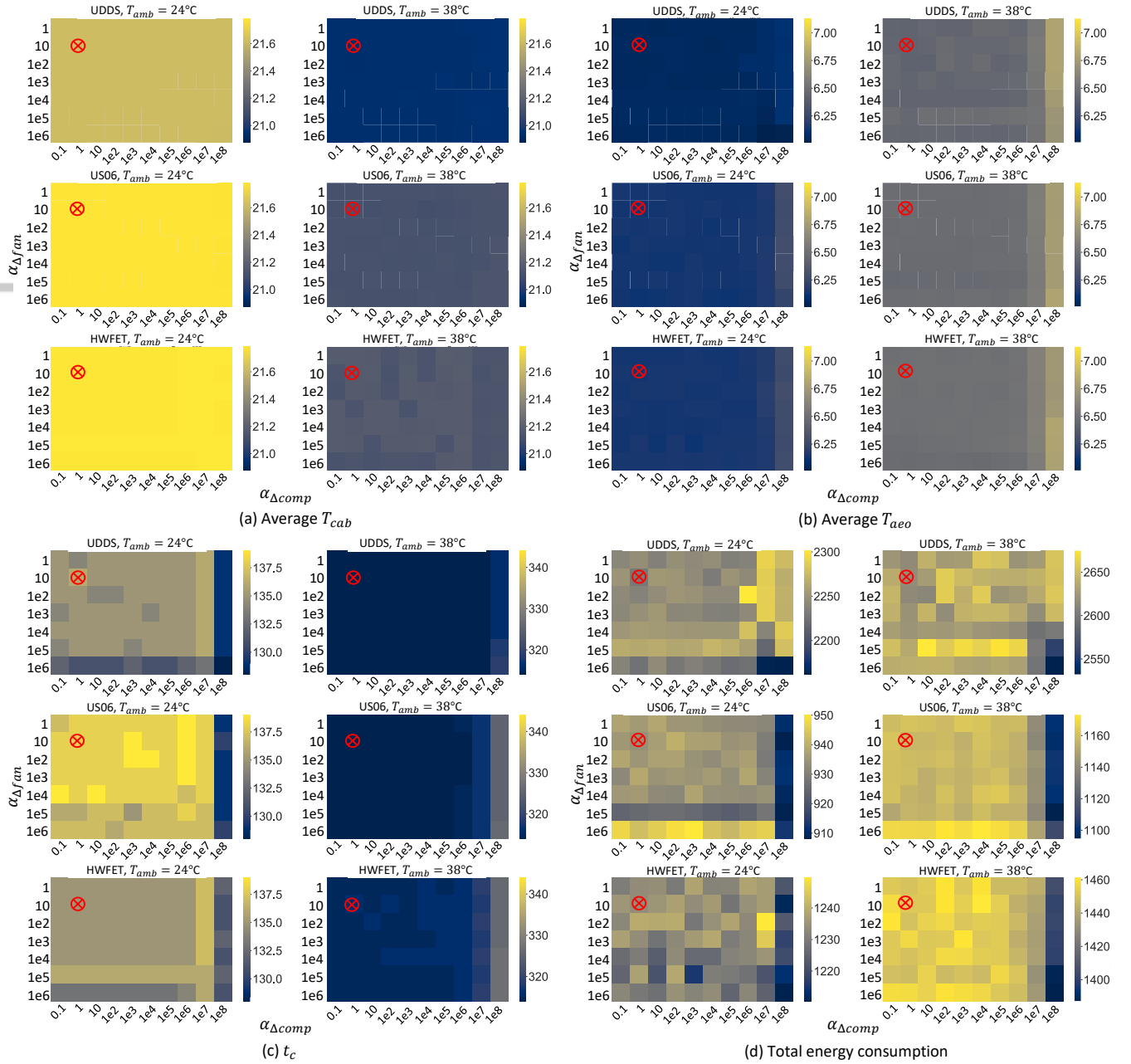


FIGURE 7 Parametric study results of $\alpha_{\Delta comp}$ and $\alpha_{\Delta fan}$: (a) average T_{cab} , (b) average $T_{aéo}$, (c) t_c , and (d) total energy consumption. The red marks represent the selected parameter combination.

- Case (3) $\alpha_{\Delta fan} = 1 \times 10^6 / \alpha_{\Delta comp} = 0.1$,
- Case (4) $\alpha_{\Delta fan} = 1 \times 10^6 / \alpha_{\Delta comp} = 1 \times 10^8$.

Figures 8(a)–(e) show the comparison of the four cases at T_{amb} of 24 °C until 400 s under the UDDS. In Fig. 8(a), T_{cab} trajectories are almost the same. However, the $T_{aéo}$ trajectories in Fig. 8(b) noticeably deviate from each other in the early stage before the temperature is regulated to the target. The T_{cab} and $T_{aéo}$ variations indicate that the trajectories of the compressor and fan vary much more than the heater among the four cases, as shown in Figs. 6 (c) to (e). In cases (2) and (4), \dot{m}_{comp} changes much faster after 25 s and results in lower $T_{aéo}$ undershooting compared to cases (1) and (3) due to the small $\alpha_{\Delta comp}$. Similarly, \dot{m}_{fan} of cases (1) and (2) changes more rapidly than that of cases (3) and (4) in between 25 s and 50 s due to the very small $\alpha_{\Delta fan}$. The

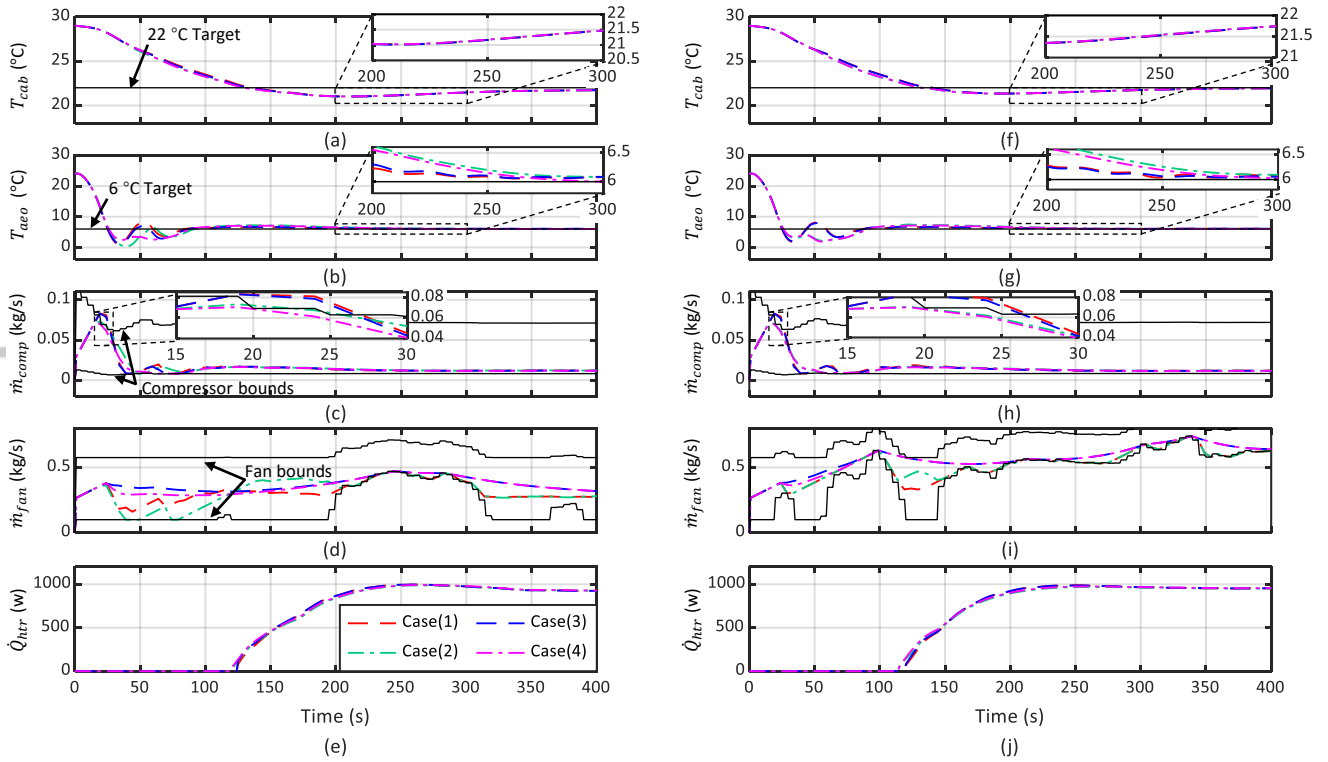


FIGURE 8 Temperature and control trajectories at 24 °C for the four cases: (a)–(e) under the UDDS and (f)–(j) under the US06

small penalty of $\Delta \dot{m}_{fan}$ in cases (1) and (2) allows a decrease in \dot{m}_{fan} to save on fan energy consumption before the raised lower bound from 195 s because the controller can quickly increase the fan operation. However, with different fan operations, different $\alpha_{\Delta comp}$ have different impacts on the compressor energy consumption, as shown in Fig. 9(a). When $\alpha_{\Delta fan}$ is small, such as in cases (1) and (2), a larger $\alpha_{\Delta comp}$ will lead to more energy consumption. This trend is because the heat transfer effectiveness at the condenser is smaller in the low \dot{m}_{fan} region (25 s to 100 s) and higher \dot{m}_{comp} is therefore needed. In this case, larger $\alpha_{\Delta comp}$ restricts the increment of \dot{m}_{comp} , which leads to an overshooting at 75 s and slightly higher energy consumption. Contrarily, when $\alpha_{\Delta fan}$ is large, \dot{m}_{fan} is kept at a relatively high value between 25 s and 100 s. As a result, lower \dot{m}_{comp} is needed because of higher heat transfer effectiveness at the condenser. In this case, no overshooting is caused by larger $\alpha_{\Delta comp}$, and less energy is used. The heater operation is very similar in each cases because $\alpha_{\Delta htr}$, $\alpha_{T_{cab}}$, and $\alpha_{T_{aero}}$ are constant.

Under the US06 cycle at T_{amb} of 24 °C, on the other hand, the T_{aero} and control trajectories shown in Figs. 8(g)–(i) are slightly different from the UDDS case. Since the vehicle speed profile of the US06 cycle is much more aggressive (higher speed and acceleration) than the UDDS cycle, the feasible range of \dot{m}_{fan} is much narrower and higher. Therefore, a larger condenser heat transfer effectiveness is achieved regardless of $\alpha_{\Delta fan}$. In this case, the situation is similar to the UDDS cases, with large $\alpha_{\Delta fan}$ and larger $\alpha_{\Delta comp}$ leading to less energy consumption. This trend can be observed in Fig. 9(b), which shows the component energy consumption under the US06 cycle. Meanwhile, with a larger $\alpha_{\Delta fan}$, the fan is utilized more since the large $\alpha_{\Delta fan}$ restricts the increment of the fan operation, and the fan cannot reach the lower bound of the narrow feasible range.

The parametric study in this subsection can be summarized as follows:

- The speed profile of the vehicle will affect the heat transfer effectiveness of the condenser, which will further influence the impact of $\alpha_{\Delta fan}$ and $\alpha_{\Delta comp}$ on the compressor and fan operation.
- Under a mild driving scenario, such as the UDDS cycle:
 - (1) with a small $\alpha_{\Delta fan}$, the larger $\alpha_{\Delta comp}$ brings more compressor utilization in the early stage;
 - (2) with a large $\alpha_{\Delta fan}$, the larger $\alpha_{\Delta comp}$ brings less compressor utilization because of more efficient condenser heat transfer;
 - (3) the larger $\alpha_{\Delta fan}$ is, the more fan utilization there will be.

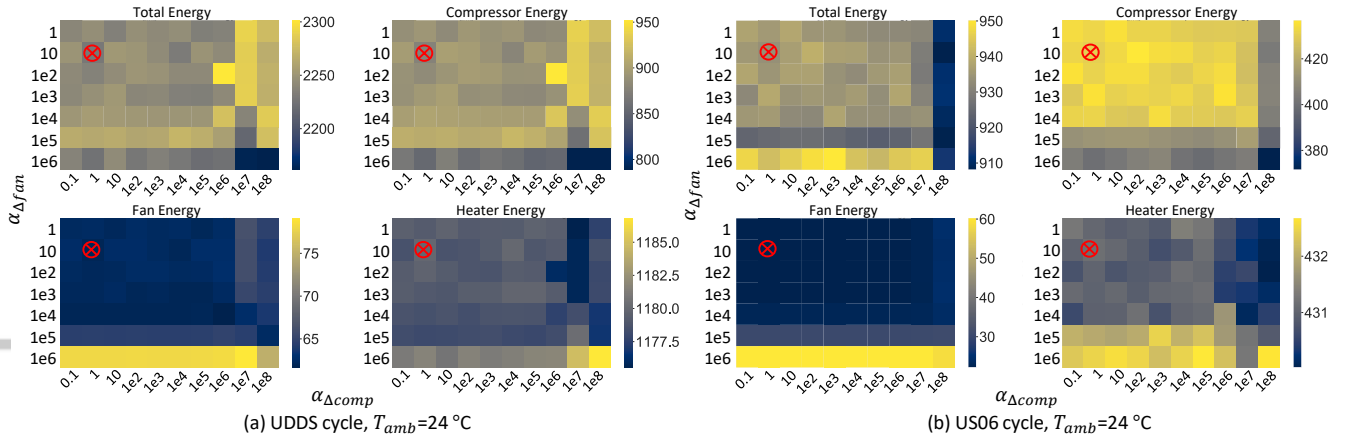


FIGURE 9 Components energy consumption results from the parametric study of $\alpha_{\Delta_{comp}}$ and $\alpha_{\Delta_{fan}}$ under the UDSS and the US06

- Under an aggressive driving scenario, such as the US06 cycle:
 - (1) the larger $\alpha_{\Delta_{comp}}$ brings less compressor utilization in the early stage because of efficient condenser heat transfer;
 - (2) the larger $\alpha_{\Delta_{fan}}$ is, the more fan utilization there will be.
- The heater operation is not affected by $\alpha_{\Delta_{fan}}$ and $\alpha_{\Delta_{comp}}$.

Although different optimal parameter sets can be found for different driving cycles, $\alpha_{\Delta_{comp}} = 1$ and $\alpha_{\Delta_{fan}} = 10$ are selected for further performance evaluations, considering the energy consumption of all six driving scenarios. The selected combination is highlighted with a red mark in Fig. 7.

4.3 | Performance Evaluation

In this subsection, the performance of the LTV-MPC controller with selected weighting factors from the parametric studies is evaluated under four driving cycles: the UDSS, the HWFET, and the US06, which are used in the parametric study to determine the optimal set of weighting factors, and the WLTC cycle, which is used for performance validation. Particularly, the LTV-MPC is compared with the NEMPC¹⁷ and the RB controller¹¹ from our previous works. These two controllers are also implemented in the MATLAB/Simulink[®] high-fidelity plant model.

The NEMPC used as the benchmark utilizes the same control-oriented HVAC model described in Section 2. Similar to the LTV-MPC, the cost function of the NEMPC includes the three power terms (the compressor, the fan, and the heater), the temperature tracking error costs (T_{cab} and T_{aao}), and the slack variable costs (T_{aao} and \dot{m}_{fan}) as follows:

$$J_{\text{NEMPC}} = \sum_{k=0}^{N_h} \left(P_{comp,k} + P_{fan,k} + P_{htr,k} + \alpha_{T_{cab}} (T_{cab,k} - T_{cab}^{target})^2 + \alpha_{T_{aao}} (T_{aao,k} - T_{aao}^{target})^2 + \alpha_{slack} (\epsilon_{T_{aao,k}}^2 + \epsilon_{\dot{m}_{fan,k}}^2) \right). \quad (30)$$

The prediction horizon, the MPC update time interval, and the sample time interval for the NEMPC are set to be identical to the LTV-MPC: 100 s, 5 s, and 5 s, respectively.

The RB controller controls the compressor speed to meet the desired T_{aao} , and the fan speed is determined by a pre-calibrated rule depending on the refrigerant pressure at the condenser and vehicle speed. The blower speed is controlled for the desired cabin cooling power computed based on the thermal loads and the T_{cab} target. Lastly, the heater is used to increase the vent outlet temperature to keep the vent outlet air temperature from being too cold.

Figure 10(a)–(c) summarizes the reference temperature tracking performance of the controllers for eight different driving conditions. In Fig. 10(a), the LTV-MPC shows that the averaged T_{cab} deviates slightly more from the 22 °C target (by 0.1 °C to 0.4 °C) but shows an averaged T_{aao} closer to the target (by 0.2 °C to 0.3 °C) when compared to the NEMPC results in all cases. When compared to the RB controller, the LTV-MPC shows a larger deviation of the averaged T_{cab} from the target (by 0.1 °C to 0.8 °C) except for the HWFET and US06 under 24 °C conditions. On the other hand, in Fig. 10(b), the RB controller shows the averaged T_{aao} closer to the target (by 0.1 °C to 0.5 °C) than the LTV-MPC except for the UDSS 38 °C and the US06

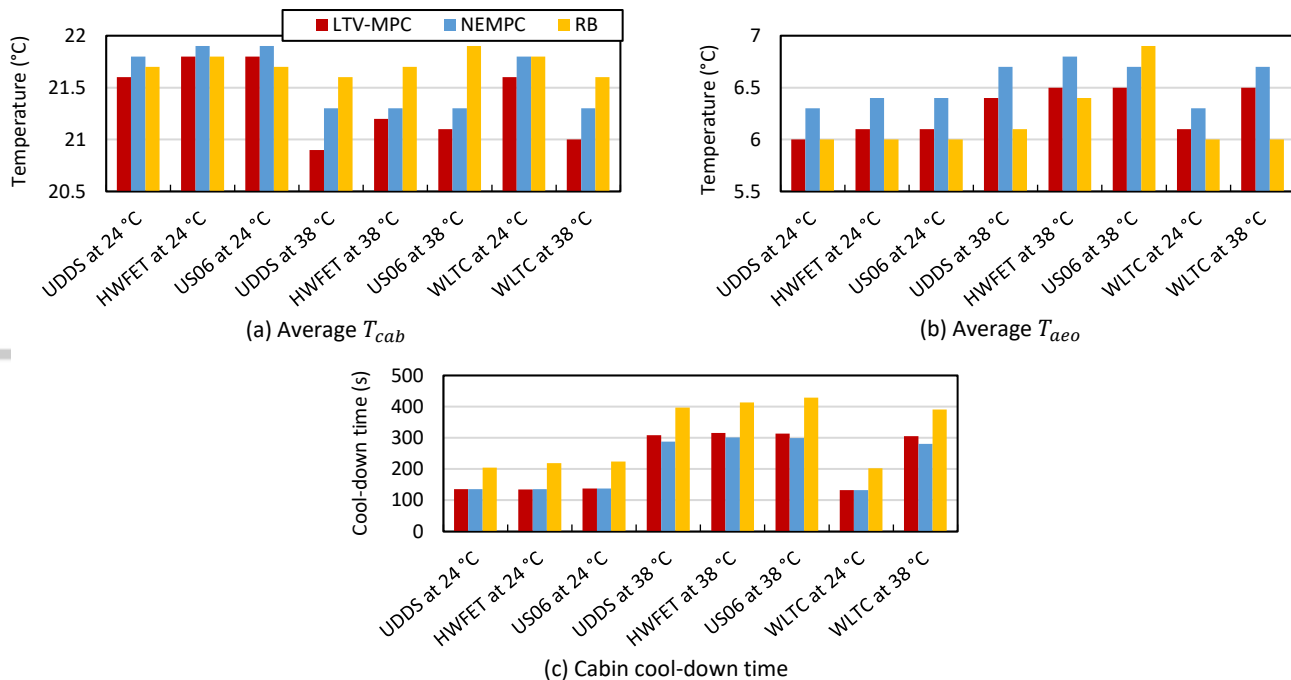


FIGURE 10 Performance evaluation of reference temperature tracking: (a) average T_{cab} , (b) average T_{aeo} and (c) cabin cool-down time

38 °C conditions. The cabin cool-down performance of the LTV-MPC shown in Fig. 10(c) is almost identical to the NEMPC at 24 °C but is 15 s to 25 s longer than at 38 °C. However, the LTV-MPC shows much faster cool-down performance than the RB controller: 69 s to 86 s faster at 24 °C and 85 s to 115 s faster at 38 °C. It can be found that the performance of the LTV-MPC is consistent over different driving cycles, including the validation cycle WLTC.

Figure 11(a)–(d) summarizes the energy consumption performance of the controllers under eight different driving conditions. In terms of the total HVAC system (Fig. 11(a)), the energy consumption of the LTV-MPC is similar to that of the NEMPC, ranging from -2.6 % to 2.5 %: more energy consumption at 38 °C, but less at 24 °C conditions, except under the WLTC, where the LTV-MPC consumes slightly more energy than NEMPC at both temperature conditions. On the other hand, the LTV-MPC consumes 3.2 % to 15.0 % less energy than the RB controller. The compressor and the fan energy consumption in Fig. 11(b)–(c) show that the LTV-MPC prefers to use the compressor a little more and to use the fan a little less compared to the NEMPC. The RB controller does not show a clear trend in the compressor and the fan usage over different conditions when compared to the LTV-MPC or the NEMPC. A noticeable and consistent trend observed over different driving conditions is that the RB utilizes the heater more than the LTV-MPC or the NEMPC, as shown in Fig. 11(d). The difference is more pronounced at 38 °C conditions. Overall, the LTV-MPC and the NEMPC save more energy than the RB controller while achieving a faster cool-down time.

Figures 12(a)–(j) show the comparison of the three controllers under the WLTC. As shown in the figure, the temperature trajectories of the LTV-MPC and the NEMPC are very similar to each other. In addition, the cool-down performance of the LTV-MPC is very close to that of the NEMPC and much faster than the RB controller in both ambient temperature conditions. The average T_{cab} and T_{aeo} of the LTV-MPC are within ± 1 °C from the targets, although T_{cab} is slightly further away from the target compared to the NEMPC or the RB controller. Especially, in 38 °C condition, the RB controller shows the best T_{cab} tracking performance compared to the LTV-MPC and the NEMPC as shown in Fig. 12(f), which is because the energy consumption of the HVAC system is much larger in the 38 °C case; thus, the penalty on the energy consumption term is relatively higher than the temperature error cost with the same weighting factors when compared to the 24 °C case. This phenomenon is more pronounced in the LTV-MPC, resulting from the lower average T_{cab} than the NEMPC. The temperature tracking performance of the LTV-MPC may be improved further by tuning weighting factors differently depending on T_{amb} .

The control trajectories obtained with the LTV-MPC and the NEMPC are shown to be very similar. Only small differences in the fan and heater operation are observed, which is because of the slight differences in the cost function and weighting factors. The results show that the LTV-MPC controller designed with the modified compressor power consumption performs comparably

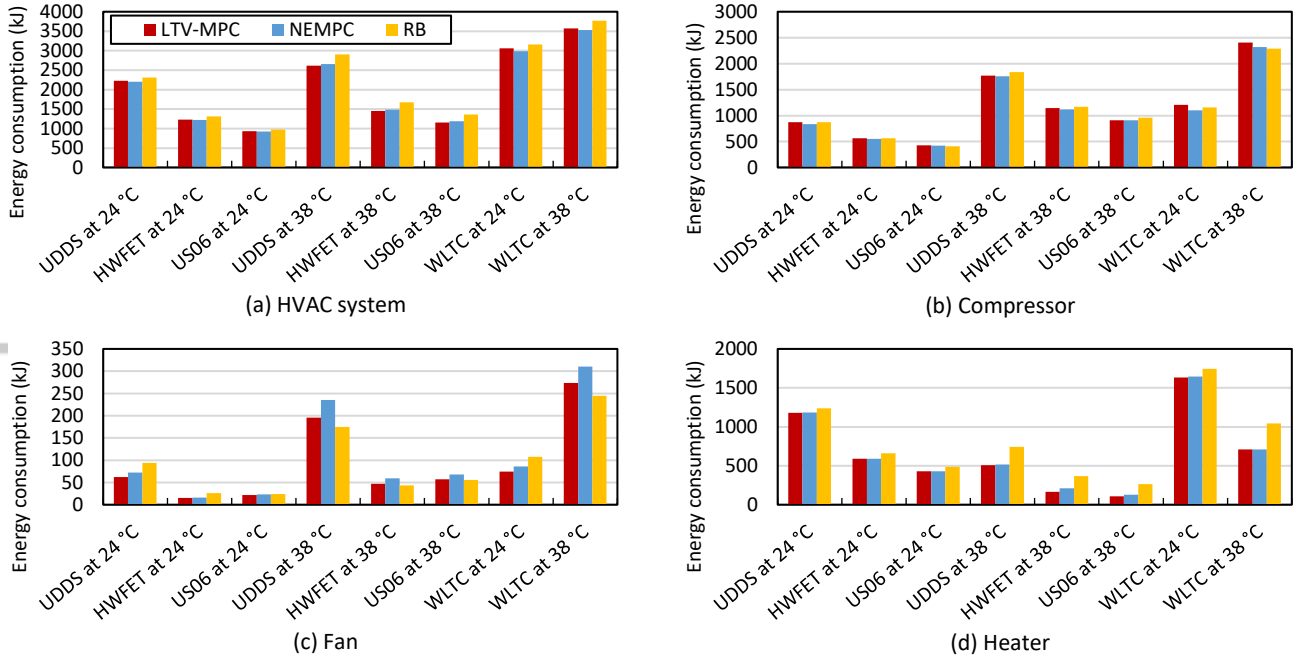


FIGURE 11 Performance evaluation of energy consumption: (a) HVAC system energy consumption, (b) compressor energy consumption, (c) fan energy consumption, and (d) heater energy consumption

to the NEMPC. While the LTV-MPC and the NEMPC show similar trajectories of the compressor, the fan, and the heater, the RB utilizes the heater more than the other two controllers, as shown in Figs. 12(e)–(j). The RB controller uses the heater in the early stage, when the cabin temperature has not yet reached the target, because the controller is not designed to consider energy consumption minimization but to avoid cold air venting out. In contrast, the LTV-MPC and the NEMPC do not utilize the heater achieving faster cool-down and saving more energy, as presented in Figs. 10 and 11.

In summary, all three controllers performed well in temperature tracking. However, the two MPC controllers perform better than the RB controller, with faster cool-down and lower energy consumption. In addition, the proposed LTV-MPC shows similar performance to the NEMPC in the WLTC driving cycle, which is not used to calibrate the weighting factors in the cost function. Comparing the results of the two MPC controllers, the average T_{cab} difference is less than 0.4 °C; the average T_{aeo} difference is less than 0.3 °C; the overall consumption difference is less than 2.6 %.

However, the computational performance is improved significantly by the LTV-MPC compared with the NEMPC. The average computation time per MPC update calculation is 97 ms in the case of the LTV-MPC, while it takes 352 ms with the NEMPC. Furthermore, the computation time is consistent among different driving conditions, with a standard deviation of 2.6 ms and 12 ms for the LTV-MPC and the NEMPC, respectively. During the LTV-MPC computation, construction of the linearization and optimization problems takes on average 3 ms and 4.6 ms, respectively. Then, the QP solver's computation time is 82.9 ms on average, and the rest of the computational time is used for the signal processing and monitoring for the LTV-MPC. In conclusion, the proposed LTV-MPC performs comparably to the NEMPC while reducing the computation time by 72.4 % on average.

5 | CONCLUSION

This paper proposes an LTV-MPC-based approach for real-time implementable cabin climate control of EVs. The proposed LTV-MPC is formulated in the form of QP since QP has been applied widely for real-time optimal control with various fast QP solvers. To express the optimal cabin climate control in QP form, the nonlinear cabin climate control model is converted into an LTV model. Also, a necessary modification is made to the compressor power consumption model that simplifies the Hessian matrix calculation by eliminating non-symmetric bi-linear terms. The error in predicting power consumption with this modification is found to remain acceptable based on the results from open-loop simulations.

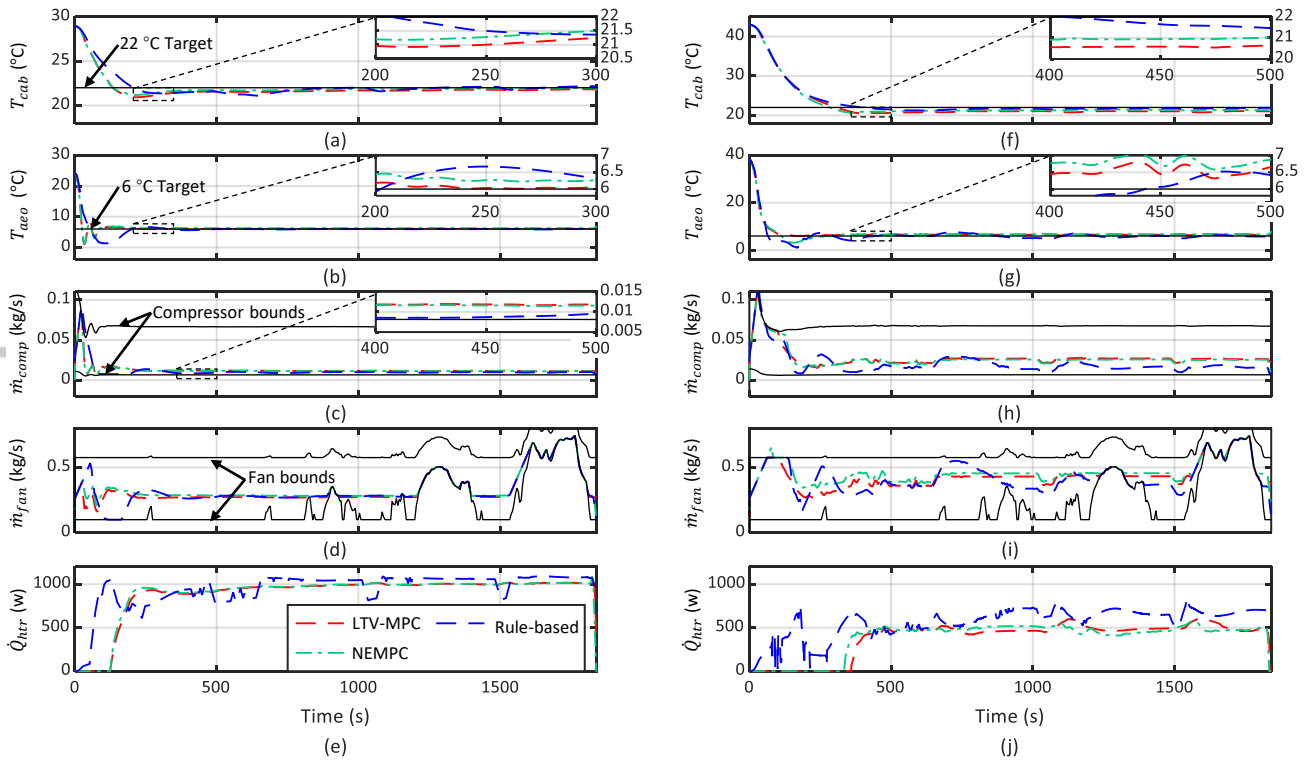


FIGURE 12 Comparison between LTV-MPC, NEMPC, and RB controllers under the WLTC cycle: (a)–(e) at T_{amb} of 24 °C and (f)–(j) at T_{amb} of 38 °C

In order to determine optimal weighting factors that work robustly under various operating conditions, a rigorous parametric study is conducted, and its results are discussed. The parametric study shows that the impact of weighting factors for the temperature regulation is influenced by the ambient temperature, while the impact of weighting factors for the control rate depends on the vehicle speed profile. Based on the results, appropriate weighting factors are selected for the cost function, and the LTV-MPC controller is evaluated and compared with the NEMPC¹⁷ and the RB controller¹¹. Compared with the RB controller, the proposed LTV-MPC reaches the target cabin temperature at least 69 s faster and using 3.2% to 15% less total HVAC system energy consumption under various driving conditions, while the averaged T_{cab} difference is 0.8 °C at most. On the other hand, the performance of the proposed LTV-MPC in temperature regulation and energy consumption is very similar to that of the NEMPC; averaged T_{cab} difference is 0.4 °C at most and the difference in total HVAC system energy consumption is within 2.6%. While maintaining the performance of the NEMPC, the LTV-MPC reduces computational time significantly, by 72.4 % on average.

In this study, two ambient temperatures are considered in the investigation. As discussed in the work by Hemmati *et al.*²⁷, complex weather conditions can affect the the HVAC system efficiency considerably. Thus, investigating various factors such as ambient temperatures, humidity, wind speed, and solar radiation variations will be one of the directions for future work. Furthermore, an exact future vehicle speed trajectory is assumed to be known for the MPC controllers in this study. Therefore, investigating the impact of imperfection in the speed profile prediction on the MPC controller's performance and robustness in traffic is also desirable for future work. Another important direction for future research will be the development of control algorithms for comprehensive vehicle thermal management, including additional relevant subsystems such as batteries and power electronics.

How to cite this article: Y. Chen, K. H. Kwak, J. Kim, Y. Kim, and D. Jung (2021), Cabin Climate Control of Electric Vehicles using Linear Time Varying Model Predictive Control, *Optim Control Appl Meth*, xxx.xxx.xxx.

APPENDIX

A COST FUNCTION IN THE QP PROBLEM

The cost function Eq. (20) in Section 3.2 can be expressed in a matrix form as follows:

$$J = \sum_{k=0}^{N_h-1} (\xi_{k+1}^T Q \xi_{k+1} + \Delta u_k^T R \Delta u_k + q_\xi \xi_{k+1}).$$

where the matrices are given by,

$$Q = \begin{bmatrix} \frac{\alpha_{T_{cab}}}{2} & 0 & 0 & \frac{a_0^*}{2} & 0 & 0 \\ 0 & 0 & 0 & \frac{a_1^*}{2} & 0 & 0 \\ 0 & 0 & 0 & 0 & 0 & 0 \\ \frac{a_0^*}{2} & \frac{a_1^*}{2} & 0 & \frac{a_2^*}{2} & \frac{a_4^*}{2} & 0 \\ 0 & 0 & 0 & \frac{a_4^*}{2} & b_1 & 0 \\ 0 & 0 & 0 & 0 & 0 & 0 \end{bmatrix}, R = \begin{bmatrix} \frac{\alpha_{\Delta_{comp}}}{2} & 0 & 0 & 0 & 0 \\ 0 & \frac{\alpha_{\Delta_{fan}}}{2} & 0 & 0 & 0 \\ 0 & 0 & \frac{\alpha_{\Delta Q}}{2} & 0 & 0 \\ 0 & 0 & 0 & \frac{\alpha_{T_{aao}}}{2} & 0 \\ 0 & 0 & 0 & 0 & \frac{\alpha_{fan}}{2} \end{bmatrix}, q_\xi = [-\alpha_{T_{cab}} \quad T_{cab,target} \quad 0 \quad 0 \quad a_3^* \quad b_2 \quad 1]. \quad (A1)$$

The matrices applied in Eq. (27) and (28) are shown in this appendix. The matrices S , M , C are expressed as follows to calculate state evolution corresponding to applied control.

$$S = \begin{bmatrix} B_{aug,0} & 0 & \dots & 0 \\ A_{aug,1} B_{aug,0} & B_{aug,1} & \dots & 0 \\ \vdots & \vdots & \ddots & \vdots \\ B_{aug,0} \Pi_{N_h-1}^1 A_{aug,k} & B_{aug,1} \Pi_{N_h-1}^2 A_{aug,k} & \dots & B_{aug,N_h-1} \end{bmatrix},$$

$$M = [A_{aug,0} \quad A_{aug,1} A_{aug,0} \quad \dots \quad \Pi_{N_h-1}^0 A_{aug,k}]^T, \quad (A2)$$

$$C = \begin{bmatrix} I_{6 \times 6} & 0 & \dots & 0 \\ A_{aug,1} & I_{6 \times 6} & \dots & 0 \\ \vdots & \vdots & \ddots & \vdots \\ \Pi_{N_h-1}^1 A_{aug,k} & \Pi_{N_h-1}^2 A_{aug,k} & \dots & I_{6 \times 6} \end{bmatrix}.$$

The cost function matrices in Eq. (A1) are stacked diagonally since the same weighting factors are applied at every time step:

$$\tilde{Q} = \begin{bmatrix} Q & 0 & \dots & 0 \\ 0 & Q & \dots & 0 \\ \vdots & \vdots & \ddots & \vdots \\ 0 & 0 & \dots & Q \end{bmatrix}, \quad \tilde{R} = \begin{bmatrix} R & 0 & \dots & 0 \\ 0 & R & \dots & 0 \\ \vdots & \vdots & \ddots & \vdots \\ 0 & 0 & \dots & R \end{bmatrix}, \quad \tilde{q}_\xi = [q_\xi \quad \dots \quad q_\xi]. \quad (A3)$$

Thus, the matrices in Eq. (27) are expressed using Eq. (A2) and Eq. (A3) as follows:

$$H = 2(S^T \tilde{Q} S + \tilde{R}),$$

$$q = 2(2\xi_0^T M^T \tilde{Q} S + 2\Phi^T C^T \tilde{Q} S + \tilde{q}_\xi S),$$

$$c = \xi_0^T M^T \tilde{Q} M \xi_0 + \Phi^T C^T \tilde{Q} C \Phi + 2\Phi^T C^T \tilde{Q} M \xi_0,$$

$$+ \tilde{q}_\xi M \xi_0 + \tilde{q}_\xi C \Phi.$$

B CONSTRAINT MATRICES IN THE QP PROBLEM

Equation (22) can be expressed in a matrix form as follows:

$$A_{temp} \xi_{k+1} + B_{temp} \Delta u_k \leq C_{temp}, \quad (B4)$$

where

$$A_{temp} = \begin{bmatrix} 0 & 1 & 0 & 0 & 0 & 0 \\ 0 & -1 & 0 & 0 & 0 & 0 \\ 0 & -1 & 0 & 0 & 0 & 0 \end{bmatrix}, \quad B_{temp} = \begin{bmatrix} 0 & 0 & 0 & -1 & 0 \\ 0 & 0 & 0 & -1 & 0 \\ 0 & 0 & 0 & 0 & 0 \end{bmatrix}, \quad C_{temp} = \begin{bmatrix} T_{a eo, target} \\ -T_{a eo, target} \\ 0 \end{bmatrix}.$$

Equation (23) can be expressed in a matrix form as follows:

$$A_{Zone} \xi_{k+1} \leq C_{Zone}, \quad (B5)$$

where

$$A_{zone} = [0 \ 0 \ 0 \ A_2 \ A_1 \ 0], \quad C_{zone} = [-A_3],$$

Equation (24) can be rearranged to the following form:

$$A_{comp} \xi_k + B_{comp} \Delta u_k \leq C_{comp}, \quad (B6)$$

where

$$A_{comp} = \begin{bmatrix} (1 - \varepsilon_e^{-1})r_{in} & \varepsilon_e^{-1} & 0 & \frac{-1}{2.224 \times 10^{-4}} & 0 & 0 \\ (\varepsilon_e^{-1} - 1)r_{in} & -\varepsilon_e^{-1} & 0 & \frac{-1}{0.0023} & 0 & 0 \end{bmatrix},$$

$$B_{comp} = \begin{bmatrix} \frac{-1}{2.224 \times 10^{-4}} & 0 & 0 & 0 & 0 \\ \frac{-1}{0.0023} & 0 & 0 & 0 & 0 \end{bmatrix},$$

$$C_{comp} = \begin{bmatrix} \frac{-0.0055}{2.224 \times 10^{-4}} - (1 - \varepsilon_e^{-1})(1 - r_{in})T_{amb} \\ \frac{-1}{0.0023} + (1 - \varepsilon_e^{-1})(1 - r_{in})T_{amb} \end{bmatrix}.$$

Equations (25) and (26) are expressed as follows:

$$A_u \xi_{k+1} + B_u \Delta u_k \leq C_u, \quad (B7)$$

$$B_{rate} \Delta u_k \leq C_{rate}, \quad (B8)$$

where

$$A_u = \begin{bmatrix} 0 & 0 & 0 & 1 & 0 & 0 \\ 0 & 0 & 0 & -1 & 0 & 0 \\ 0 & 0 & 0 & 0 & 1 & 0 \\ 0 & 0 & 0 & 0 & -1 & 0 \\ 0 & 0 & 0 & 0 & 0 & 1 \\ 0 & 0 & 0 & 0 & 0 & -1 \end{bmatrix}, \quad B_u = \begin{bmatrix} 0 & 0 & 0 & 0 & 0 \\ 0 & 0 & 0 & 0 & 0 \\ 0 & 0 & 0 & 0 & -1 \\ 0 & 0 & 0 & 0 & -1 \\ 0 & 0 & 0 & 0 & 0 \\ 0 & 0 & 0 & 0 & 0 \end{bmatrix}, \quad C_u = \begin{bmatrix} 0.125 \\ -0.005 \\ fan_{max} \\ -fan_{min} \\ 5000 \\ 0 \end{bmatrix},$$

$$A_{rate} = \begin{bmatrix} 1 & 0 & 0 & 0 & 0 \\ -1 & 0 & 0 & 0 & 0 \\ 0 & 1 & 0 & 0 & 0 \\ 0 & -1 & 0 & 0 & 0 \\ 0 & 0 & 1 & 0 & 0 \\ 0 & 0 & -1 & 0 & 0 \\ 0 & 0 & 0 & -1 & 0 \\ 0 & 0 & 0 & 0 & -1 \end{bmatrix}, \quad C_{rate} = \begin{bmatrix} 0.003 \\ 0.006 \\ 0.005 \\ 0.02 \\ 100 \\ 100 \\ 0 \\ 0 \end{bmatrix} \Delta t.$$

The inequality constraints Eq. (B4), (B5), (B6), (B7), and (B8) are further expressed respectively in QP form by stacking elements diagonally in Eq. (B9), (B10), (B11), (B12), and (B13):

$$\left(\begin{bmatrix} A_{comp} & \dots & 0 & 0 \\ \vdots & \ddots & \vdots & \vdots \\ 0 & \dots & A_{comp} & 0 \end{bmatrix} S + \begin{bmatrix} 0 & B_{comp} & \dots & 0 \\ \vdots & \vdots & \ddots & \vdots \\ 0 & 0 & \dots & B_{comp} \end{bmatrix} \right) U \leq \begin{bmatrix} C_{comp} \\ \vdots \\ C_{comp} \end{bmatrix} - \begin{bmatrix} A_{comp} & \dots & 0 & 0 \\ \vdots & \ddots & \vdots & \vdots \\ 0 & \dots & A_{comp} & 0 \end{bmatrix} M \xi_0, \quad (B9)$$

$$[B_{comp}] [I_{5 \times 5} \ 0 \ \dots \ 0] U \leq [C_{comp}] - [A_{comp}] \xi_0,$$

$$([A_{temp}|_{N \times N}] S + [B_{temp}|_{N \times N}]) U \leq [C_{temp}|_{N \times 1}] - [A_{temp}|_{N \times N}] M \xi_0, \quad (B10)$$

$$[A_{zone}|_{N \times N}] S U \leq [C_{zone}|_{N \times 1}] - [A_{zone}|_{N \times N}] M \xi_0, \quad (B11)$$

$$[A_u|_{N \times N}] S U \leq [C_u|_{N \times 1}] - [A_u|_{N \times N}] M \xi_0, \quad (B12)$$

$$[B_{rate}|_{N \times N}] U \leq [C_{rate}|_{N \times 1}]. \quad (B13)$$

The matrices G , W , T applied in Eq. (27) are expressed as follows, combining Eq. (B9), (B10), (B11), (B12), and (B13).

$$G = \begin{bmatrix} \begin{bmatrix} A_{comp1} & \dots & 0 & 0 \\ \vdots & \ddots & \vdots & \vdots \\ 0 & \dots & A_{comp1} & 0 \end{bmatrix} S + \begin{bmatrix} 0 & B_{comp1} & \dots & 0 \\ \vdots & \vdots & \ddots & \vdots \\ 0 & 0 & \dots & B_{comp1} \end{bmatrix} \\ \begin{bmatrix} A_{comp2} & \dots & 0 & 0 \\ \vdots & \ddots & \vdots & \vdots \\ 0 & \dots & A_{comp2} & 0 \end{bmatrix} S + \begin{bmatrix} 0 & B_{comp2} & \dots & 0 \\ \vdots & \vdots & \ddots & \vdots \\ 0 & 0 & \dots & B_{comp2} \end{bmatrix} \\ \begin{bmatrix} B_{comp1} \\ B_{comp2} \end{bmatrix} [I_{5 \times 5} \ 0 \ \dots \ 0] \\ \begin{bmatrix} A_{temp} & \dots & 0 \\ \vdots & \ddots & \vdots \\ 0 & \dots & A_{temp} \end{bmatrix} S + \begin{bmatrix} B_{temp} & \dots & 0 \\ \vdots & \ddots & \vdots \\ 0 & \dots & B_{temp} \end{bmatrix} \\ \begin{bmatrix} A_{zone} & \dots & 0 \\ \vdots & \ddots & \vdots \\ 0 & \dots & A_{zone} \end{bmatrix} S \\ \begin{bmatrix} A_u & \dots & 0 \\ \vdots & \ddots & \vdots \\ 0 & \dots & A_u \end{bmatrix} S \\ \begin{bmatrix} A_{rate} & \dots & 0 \\ \vdots & \ddots & \vdots \\ 0 & \dots & A_{rate} \end{bmatrix} \end{bmatrix}, \quad W = \begin{bmatrix} C_{comp1} \\ \vdots \\ C_{comp1} \\ C_{comp2} \\ \vdots \\ C_{comp2} \\ C_{temp} \\ \vdots \\ C_{temp} \\ C_{zone} \\ \vdots \\ C_{zone} \\ C_u \\ \vdots \\ C_u \\ C_{rate} \\ \vdots \\ C_{rate} \end{bmatrix}, \quad T = - \begin{bmatrix} \begin{bmatrix} A_{comp1} & \dots & 0 & 0 \\ \vdots & \ddots & \vdots & \vdots \\ 0 & \dots & A_{comp1} & 0 \end{bmatrix} M \\ \begin{bmatrix} A_{comp2} & \dots & 0 & 0 \\ \vdots & \ddots & \vdots & \vdots \\ 0 & \dots & A_{comp2} & 0 \end{bmatrix} M \\ \begin{bmatrix} A_{temp} & \dots & 0 \\ \vdots & \ddots & \vdots \\ 0 & \dots & A_{temp} \end{bmatrix} M \\ \begin{bmatrix} A_{zone} & \dots & 0 \\ \vdots & \ddots & \vdots \\ 0 & \dots & A_{zone} \end{bmatrix} M \\ \begin{bmatrix} A_u & \dots & 0 \\ \vdots & \ddots & \vdots \\ 0 & \dots & A_u \end{bmatrix} M \\ \begin{bmatrix} 0 & \dots & 0 \\ \vdots & \ddots & \vdots \\ 0 & \dots & 0 \end{bmatrix} \end{bmatrix}. \quad (B14)$$

DATA AVAILABILITY STATEMENT

The data that support the findings of this study are available from the corresponding author upon reasonable request.

References

- Hall D, Cui H, Lutsey N. Electric vehicle capitals: Showing the path to a mainstream market. International Council on Clean Transportation, Washington, D.C., USA; 2019.
- Pevec D, Babic J, Carvalho A, Ghiassi-Farrokhfal Y, Ketter W, Podobnik V. A survey-based assessment of how existing and potential electric vehicle owners perceive range anxiety. *Journal of Cleaner Production* 2020; 276: 122779. doi: 10.1016/j.jclepro.2020.122779

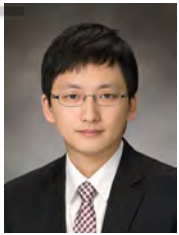
3. Khoury GE, Clodic D. Method of Test and Measurements of Fuel Consumption Due to Air Conditioning Operation on the New Prius II Hybrid Vehicle. In: SAE Technical Paper 2005-01-2049. ; 2005: 2005–01–2049
4. Lee JT, Kwon S, Lim Y, Chon MS, Kim D. Effect of Air-Conditioning on Driving Range of Electric Vehicle for Various Driving Modes. In: SAE Technical Paper 2013-01-0040. ; 2013: 2013–01–0040
5. Farrington R, Rugh J. Impact of Vehicle Air-Conditioning on Fuel Economy, Tailpipe Emissions, and Electric Vehicle Range: Preprint. 2000.
6. Uematsu S, Uehara T, Uchida T, Mathur GD. Experimental Investigation of Factors Affecting Odors Generating from Mobile AC Systems Equipped with Idling-Time Reduction Systems. *SAE International Journal of Passenger Cars - Mechanical Systems* 2015; 8(2): 399–404. doi: 10.4271/2015-01-0359
7. Menken JC, Strasser K, Anzenberger T, Rebinger C. Evaluation of the Energy Consumption of a Thermal Management System of a Plug-In Hybrid Electric Vehicle Using the Example of the Audi Q7 e-tron. *SAE International Journal of Passenger Cars - Mechanical Systems* 2018; 11(3): 203–212. doi: 10.4271/06-11-03-0017
8. Schaut S, Sawodny O. Thermal Management for the Cabin of a Battery Electric Vehicle Considering Passengers' Comfort. *IEEE Transactions on Control Systems Technology* 2020; 28(4): 1476-1492. doi: 10.1109/TCST.2019.2914888
9. Ibrahim BSKK, Aziah MAN, Ahmad S, et al. Fuzzy-based Temperature and Humidity Control for HV AC of Electric Vehicle. *Procedia Engineering* 2012; 41: 904–910. doi: 10.1016/j.proeng.2012.07.261
10. Lajunen A, Yang Y, Emadi A. Review of Cabin Thermal Management for Electrified Passenger Vehicles. *IEEE Transactions on Vehicular Technology* 2020; 69(6): 6025–6040. Conference Name: IEEE Transactions on Vehicular Technology.
11. Kim J, Rodriguez R, Kwak KH, Jung D, Kim Y. The Effect of Driver's Behavior and Environmental Conditions on Thermal Management of Electric Vehicles. In: SAE Technical Paper. ; 2020. No. 2020-01-1382
12. Rostiti C, Stockar S, Canova M. A Rule-Based Control for Fuel-Efficient Automotive Air Conditioning Systems. In: SAE Technical Paper 2015-01-0366. ; 2015: 2015–01–0366
13. Zhang Q, Fiorentini L, Canova M. H_∞ robust control of an automotive air conditioning system. In: American Control Conference. ; 2014; Portland, OR, USA
14. Wang H, Amini MR, Hu Q, Kolmanovsky I, Sun J. Eco-Cooling Control Strategy for Automotive Air-Conditioning System: Design and Experimental Validation. *IEEE Transactions on Control Systems Technology* 2020: 1-12. doi: 10.1109/TCST.2020.3038746
15. Wang H, Meng Y, Zhang Q, et al. MPC-Based Precision Cooling Strategy (PCS) for Efficient Thermal Management of Automotive Air Conditioning System. In: The 3rd IEEE Conference on Control Technology and Applications (CCTA). ; 2019; Hong Kong, China.
16. Glos J, Otava L, Václavěk P. Non-Linear Model Predictive Control of Cabin Temperature and Air Quality in Fully Electric Vehicles. *IEEE Transactions on Vehicular Technology* 2021; 70(2): 1216–1229. doi: 10.1109/TVT.2021.3054170
17. Kwak KH, Kim J, Chen Y, Kim Y, Jung D. Economic Model Predictive Control of HVAC System in Electric Vehicles. In: Modeling, Estimation and Control Conference. ; 2021; Austin TX USA. (Accepted).
18. Wang Y, Boyd S. Fast Model Predictive Control Using Online Optimization. *IEEE Transactions on Control Systems Technology* 2010; 18(2): 267–278. doi: 10.1109/TCST.2009.2017934
19. Bemporad A. A Numerically Stable Solver for Positive Semidefinite Quadratic Programs Based on Nonnegative Least Squares. *IEEE Transactions on Automatic Control* 2018; 63(2): 525–531. Conference Name: IEEE Transactions on Automatic Controldoi: 10.1109/TAC.2017.2735938
20. Docimo DJ, Pangborn HC, Alleyne AG. Hierarchical Control for Electro-Thermal Power Management of an Electric Vehicle Powertrain. In: ASME Dynamic Systems and Control Conference. ; 2018; Atlanta, Georgia, USA: V002T19A010

21. Xie Y, Liu Z, Li K, et al. An improved intelligent model predictive controller for cooling system of electric vehicle. *Applied Thermal Engineering* 2021; 182: 116084. doi: 10.1016/j.applthermaleng.2020.116084
22. Prášek J, Trnka P, Havlena V, McGahan P. Range control MPC with application to Vapor Compression Cycles. *Control Engineering Practice* 2020; 96: 104309. doi: 10.1016/j.conengprac.2020.104309
23. Pčolka M, Žáčková E, Robinett R, Čelikovský S, Sebek M. From Linear to Nonlinear Model Predictive Control of a Building. *IFAC Proceedings Volumes* 2014; 47(3): 587–592. doi: 10.3182/20140824-6-ZA-1003.02783
24. Amini MR, Kolmanovsky I, Sun J. Hierarchical MPC for Robust Eco-Cooling of Connected and Automated Vehicles and Its Application to Electric Vehicle Battery Thermal Management. *IEEE Transactions on Control Systems Technology* 2021; 29(1): 316–328. doi: 10.1109/TCST.2020.2975464
25. Kim J. *A Study on Development of Simulation Model and Model-based Predictive Control Algorithm for Electric Vehicle Thermal Management System*. Ph.D. Dissertation, Department of Mechanical Engineering. Sejong University, South Korea; 2019.
26. Ferreau H, Kirches C, Potschka A, Bock H, Diehl M. qpOASES: A parametric active-set algorithm for quadratic programming. *Mathematical Programming Computation* 2014; 6(4): 327–363.
27. Hemmati S, Doshi N, Hanover D, Morgan C, Shahbakhti M. Integrated cabin heating and powertrain thermal energy management for a connected hybrid electric vehicle. *Applied Energy* 2021; 283: 116353. doi: 10.1016/j.apenergy.2020.116353

AUTHOR BIOGRAPHY



Youyi Chen received his B.S degree from Xi'an Jiaotong University, China in 2018 and the M.S.E degree in mechanical engineering from University of Michigan-Dearborn, MI USA, in 2020. He is currently a Ph.D student with the Department of Mechanical Engineering at the University of Michigan-Dearborn. His research interests are in optimal thermal management of electric vehicles.



Kyoung Hyun Kwak is currently an Assistant Research Scientist with the Department of Mechanical Engineering at the University of Michigan-Dearborn. He received his B.S degree from Seoul National University, Korea in 2008 and the M.S.E and the Ph.D. degrees in mechanical engineering from the University of Michigan, Ann Arbor, MI USA, in 2011 and 2014, respectively. His research interests include modeling advanced internal combustion engines and vehicle powertrain systems, modeling/controlling vehicle thermal management systems of internal combustion engines and electrified vehicles, and optimizing energy storage systems.



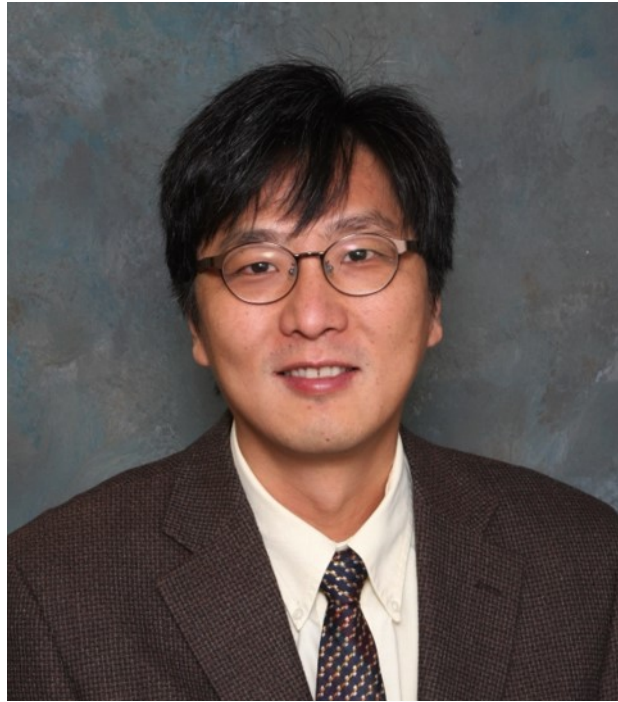
Jaewoong Kim is a Senior Research Engineer of in the R&D division of Hyundai-Kia Motor Company. He has researched and developed a vehicle thermal management system including HVAC, PE and battery and the control algorithms, over 18 years. He received his B.S. and M.S. degrees from Ulsan University, Korea in 2001 and 2003, respectively, and the Ph.D. degree from the Sejong University, Korea in 2019, all in mechanical engineering. His research interests are modeling and integrating optimal control of vehicle thermal management systems at the vehicle level in electric vehicles .



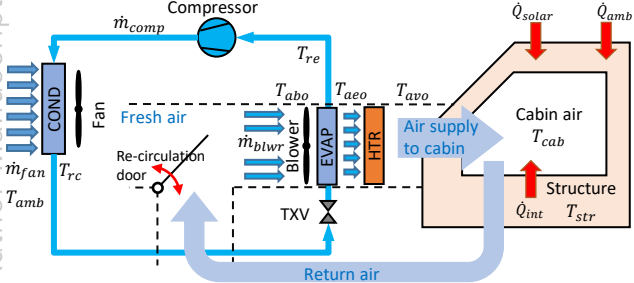
Youngki Kim received the B.S. and M.S. degrees from Seoul National University, South Korea, in 2001 and 2003, respectively, and the Ph.D. degree from the University of Michigan, Ann Arbor, MI USA, in 2014, all in mechanical engineering. He is currently an Assistant Professor with the Department of Mechanical Engineering at the University of Michigan-Dearborn (UM-Dearborn). Prior to joining the UM-Dearborn, he was a Research Engineer at Ann Arbor Technical Center, Southwest Research Institute from 2015 to 2017. He was with Hyundai-Kia Motor Company from 2003 to 2008 as a Research Engineer. Dr. Kim is the recipient of the SAE Russell S. Springer award (2019) from SAE International. His research interests include modeling and estimation/control of electrified powertrain systems, connected and automated vehicles, and energy storage systems.

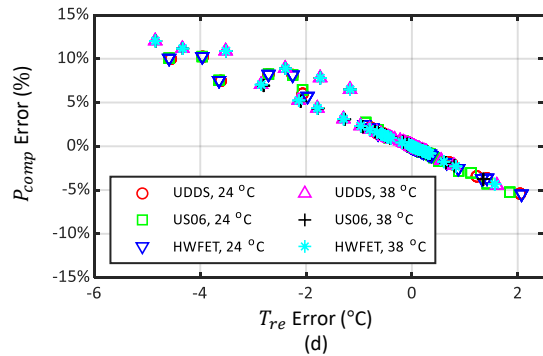
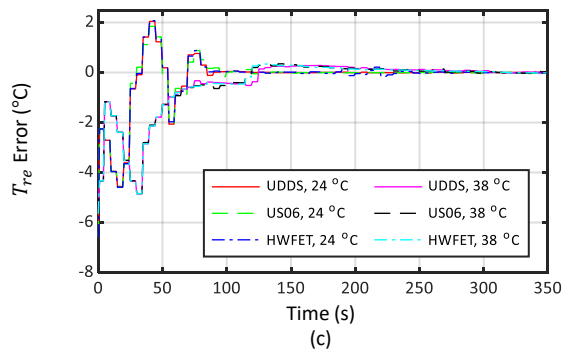
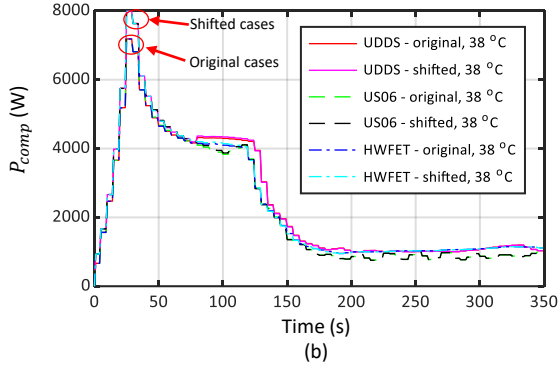
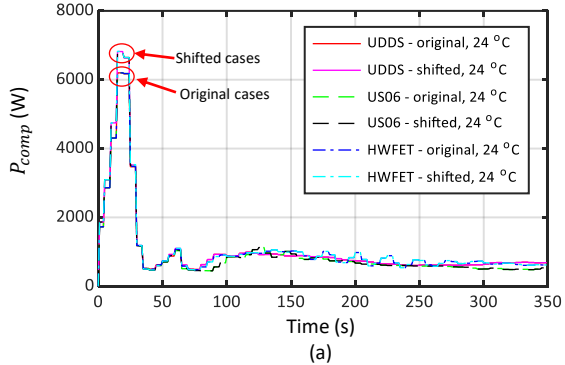


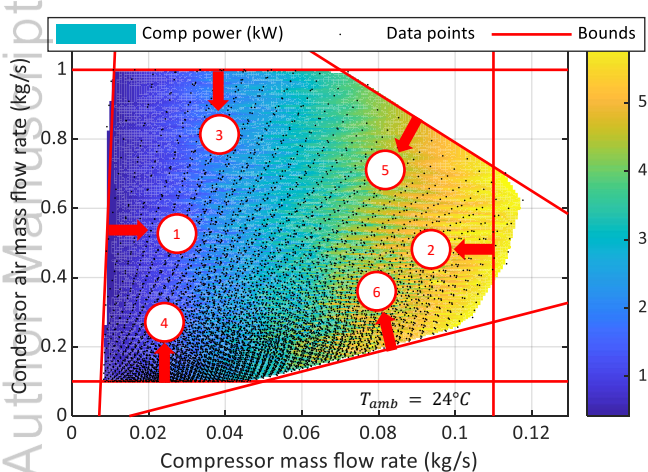
Dewey Jung is a Professor in the Department of Mechanical Engineering at the University of Michigan-Dearborn. He has over 30 years of academic and professional experience in mechanical and automotive engineering. He received his Ph.D. degree from the University of Michigan (Ann Arbor campus) in 2001 and B.S. and M.S. degrees from Seoul National University in Korea in 1989 and 1991, respectively. Dr. Jung is the recipient of the Distinguished Research Award from the University of Michigan-Dearborn (2012). His research interest has been focused on thermal and fluid sciences and their applications to advanced energy conversion systems in automotive applications, including internal combustion engine processes and systems, hybrid/electric powertrain systems; fuel cell systems; vehicle thermal and energy management; solar energy systems; and integration, modeling, and simulation of vehicle systems.

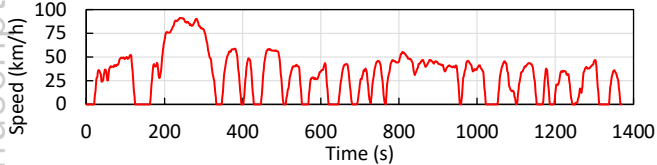


DJung.jpg

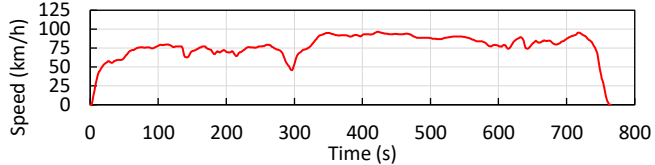




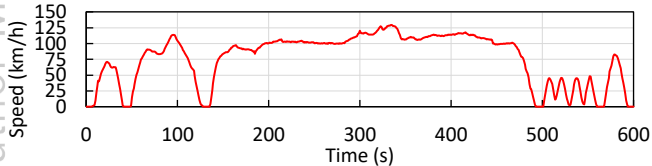




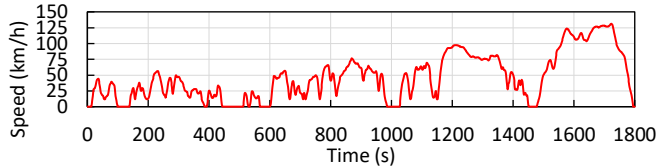
(a) Urban dynamometer driving schedule



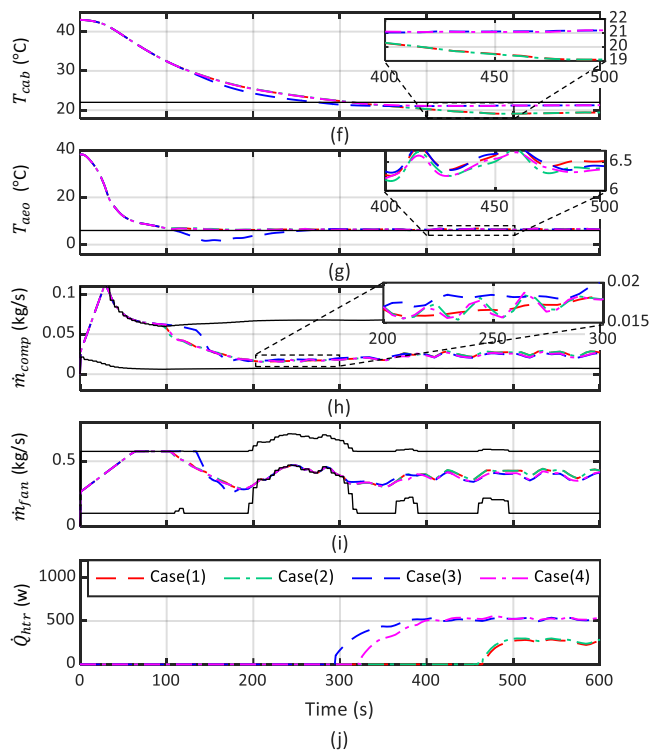
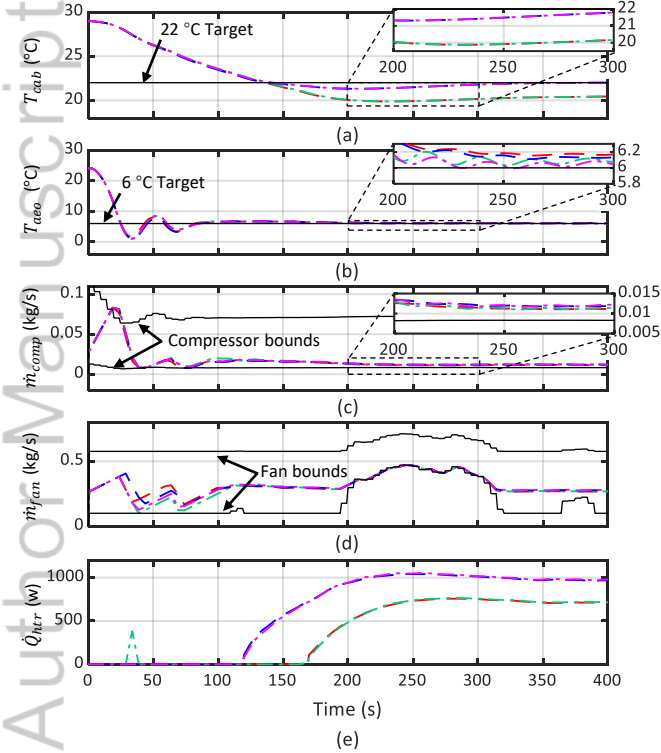
(b) Highway fuel economy test cycle

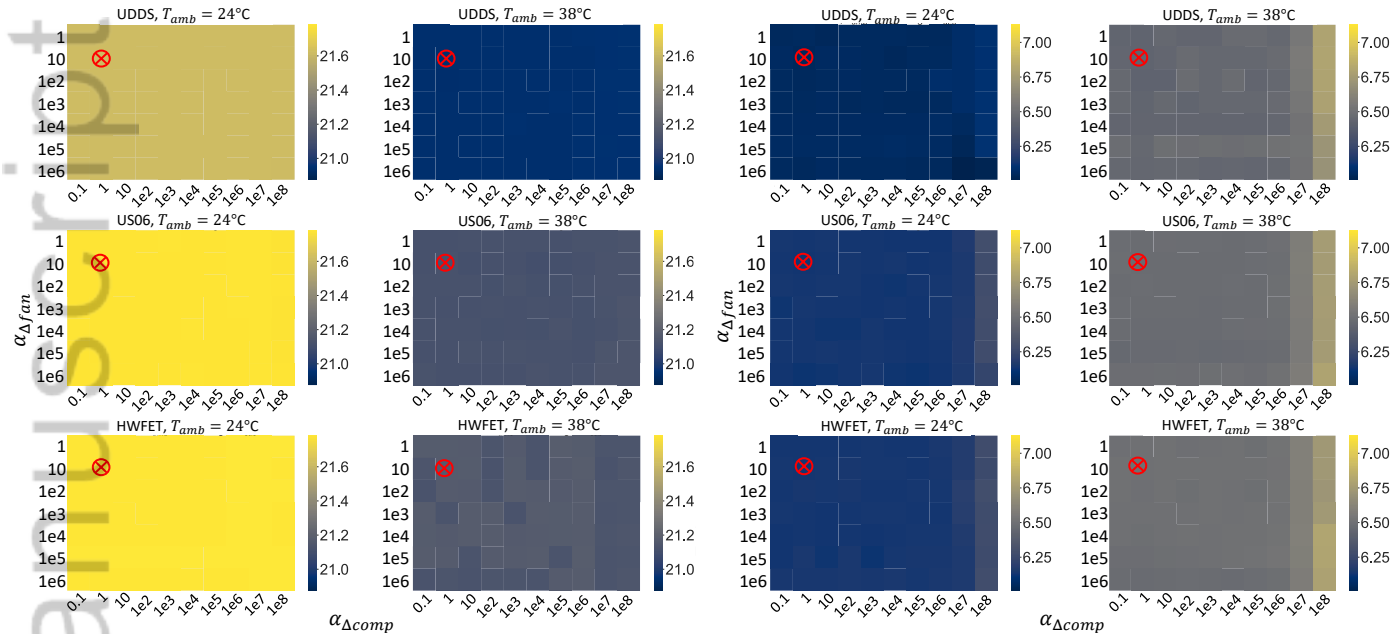
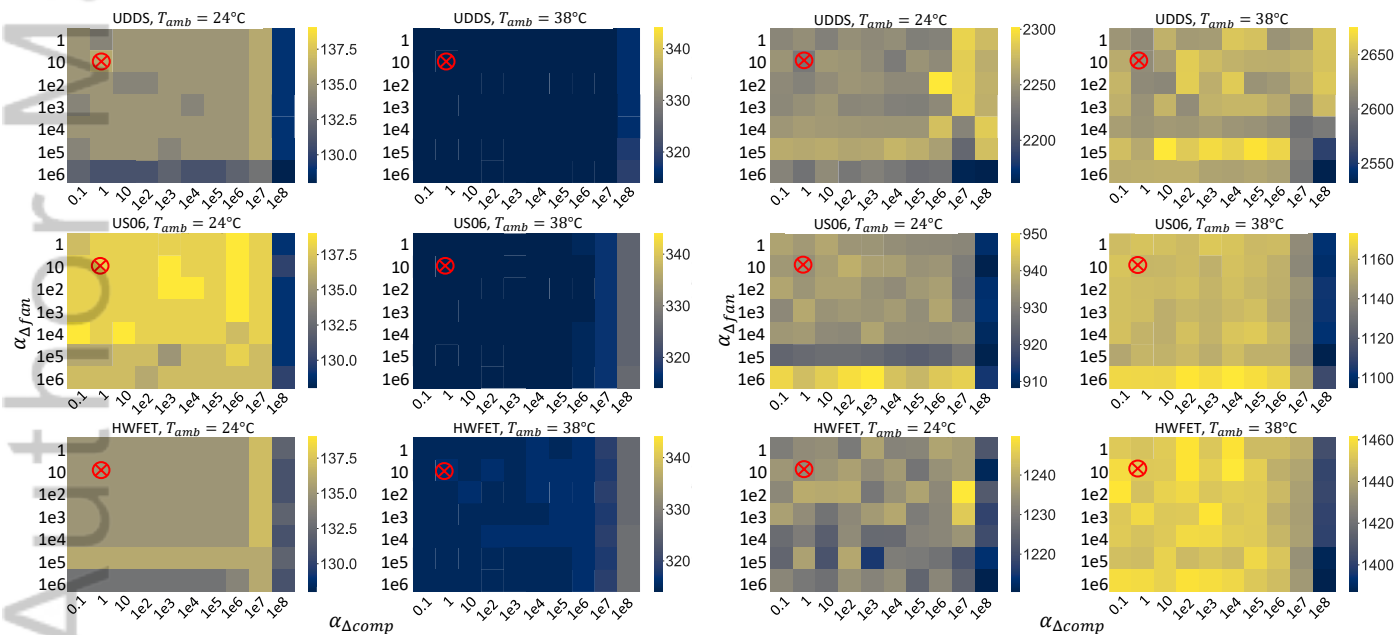


(c) US06 driving cycle

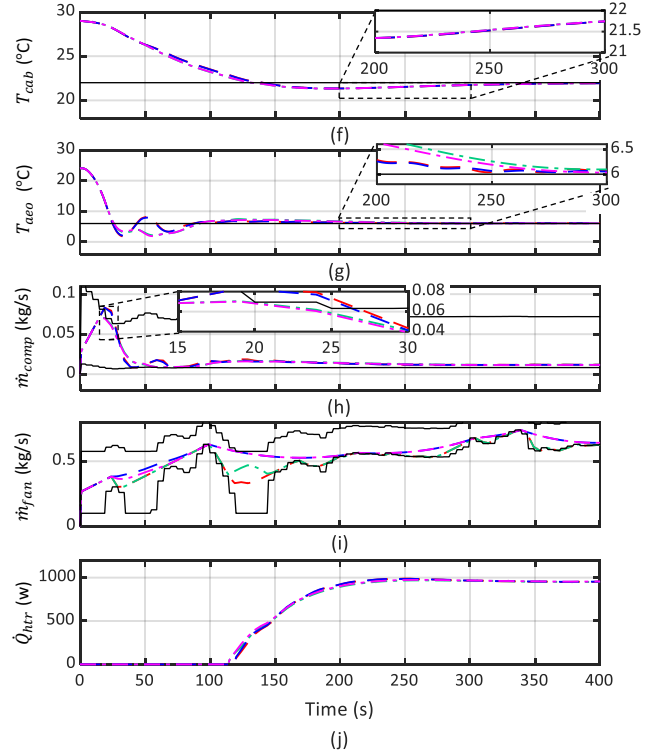
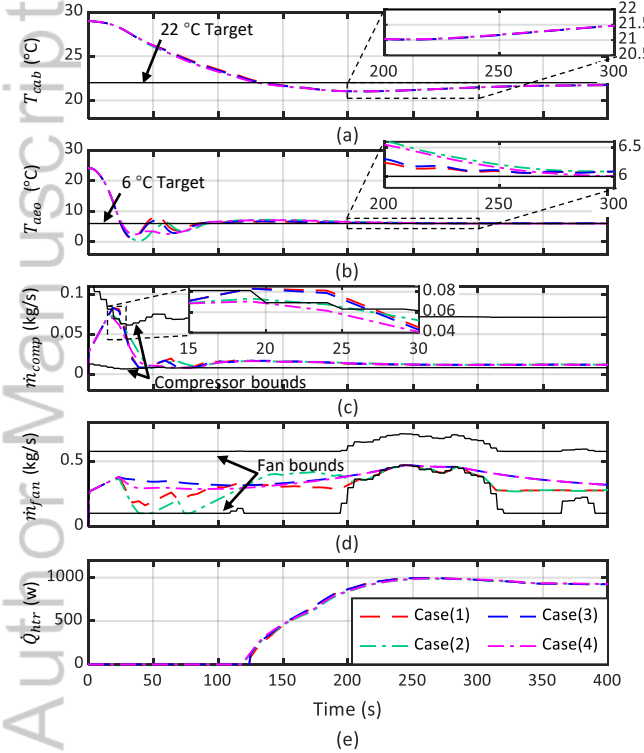


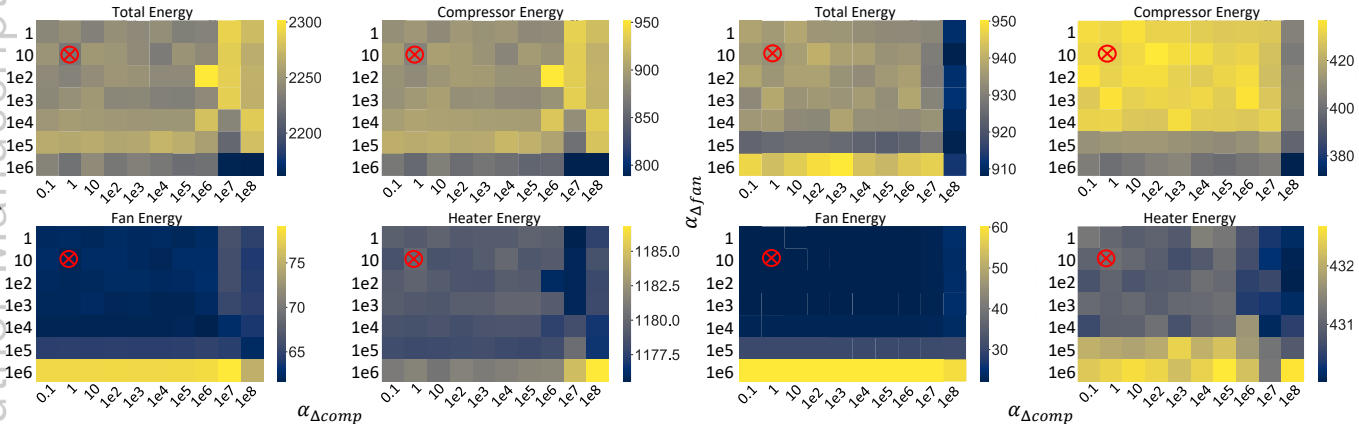
(d) Worldwide harmonized light vehicles test cycle

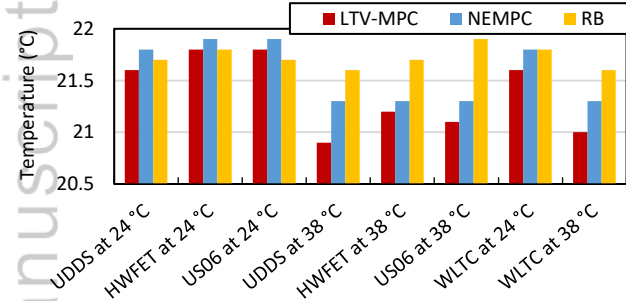
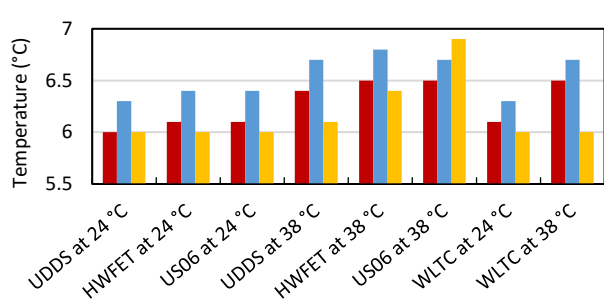
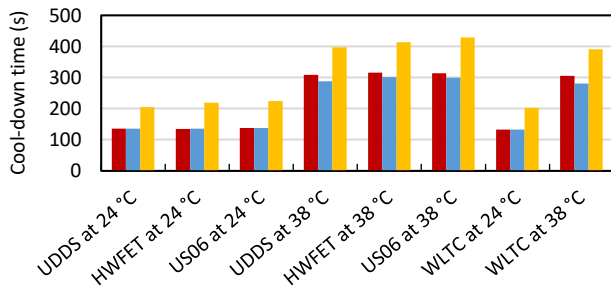


(a) Average T_{cab} (b) Average T_{aero} (c) t_c

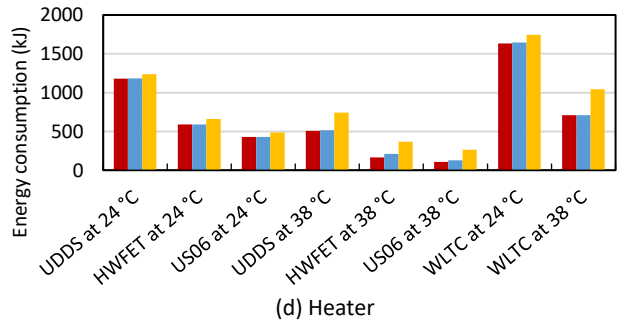
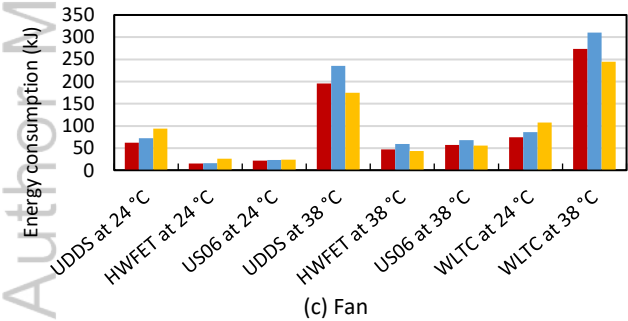
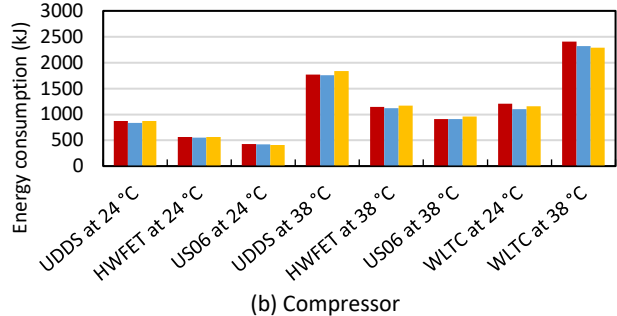
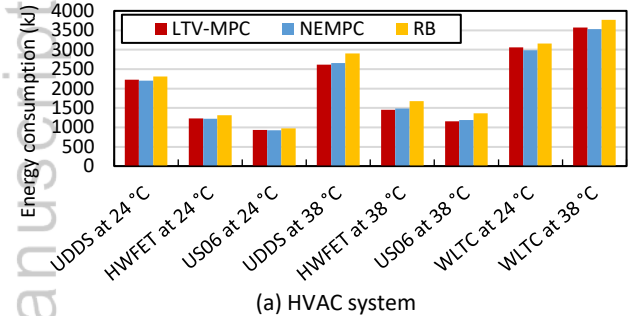
(d) Total energy consumption

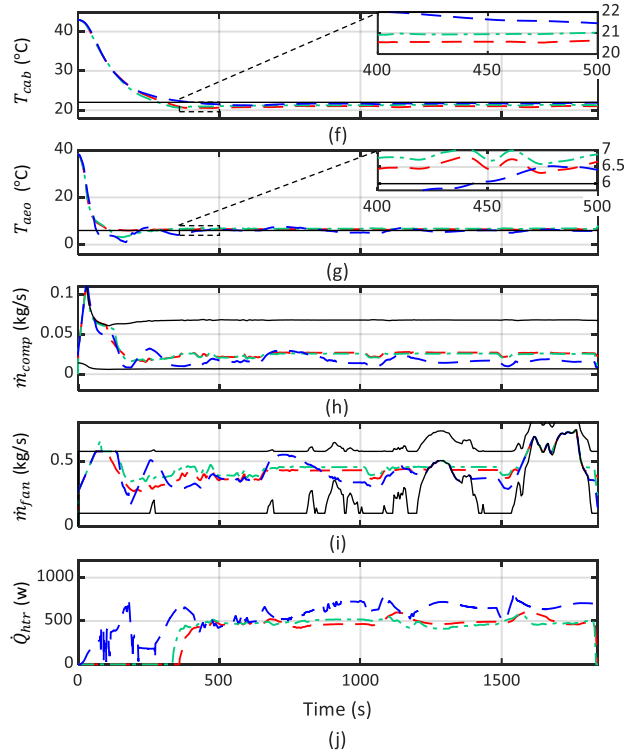
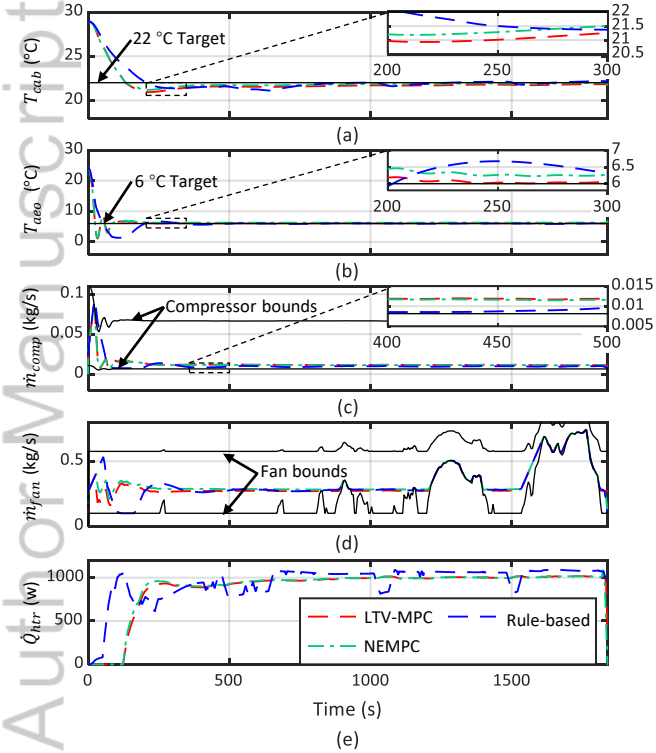


(a) UDDS cycle, $T_{amb} = 24^\circ\text{C}$ (b) US06 cycle, $T_{amb} = 24^\circ\text{C}$

(a) Average T_{cab} (b) Average T_{aeo} 

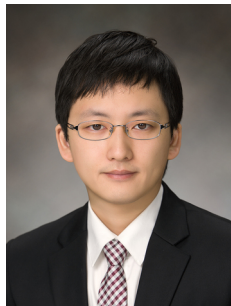
(c) Cabin cool-down time







jwKim_scr.jpg



KH_Kwak.jpg



YKim.jpg



YouyiChen_resize.jpg